



This is a repository copy of *Secondary electron spectra of semi-crystalline polymers – a novel polymer characterisation tool?*.

White Rose Research Online URL for this paper:

<https://eprints.whiterose.ac.uk/120508/>

Version: Accepted Version

Article:

Dapor, M., Masters, R., Ross, I. et al. (9 more authors) (2018) Secondary electron spectra of semi-crystalline polymers – a novel polymer characterisation tool? *Journal of Electron Spectroscopy and Related Phenomena*, 222. pp. 95-105. ISSN 0368-2048

<https://doi.org/10.1016/j.elspec.2017.08.001>

Article available under the terms of the CC-BY-NC-ND licence
(<https://creativecommons.org/licenses/by-nc-nd/4.0/>).

Reuse

This article is distributed under the terms of the Creative Commons Attribution-NonCommercial-NoDerivs (CC BY-NC-ND) licence. This licence only allows you to download this work and share it with others as long as you credit the authors, but you can't change the article in any way or use it commercially. More information and the full terms of the licence here: <https://creativecommons.org/licenses/>

Takedown

If you consider content in White Rose Research Online to be in breach of UK law, please notify us by emailing eprints@whiterose.ac.uk including the URL of the record and the reason for the withdrawal request.



eprints@whiterose.ac.uk
<https://eprints.whiterose.ac.uk/>

“Secondary electron spectra of semi-crystalline polymers – a novel polymer characterisation tool?”

Maurizio Dapor¹, Robert C. Masters², Ian Ross³, David Lidzey⁴, Andrew Pearson⁵, Isabel Abril⁶, Rafael Garcia-Molina⁷, Jo Sharp², Marek Unčovský⁸, Tomas Vystavel⁸, Filip Mika⁹, Cornelia Rodenburg²

¹European Centre for Theoretical Studies in Nuclear Physics and Related Areas (ECT*-FBK) and Trento Institute for Fundamental Physics and Applications (TIFPA-INFN), via Sommarive 18, I-38123 Trento, Italy

²Department of Materials Science and Engineering, University of Sheffield, Mappin Street, Sheffield S1 3JD, UK

³Department of Electronic and Electrical Engineering, University of Sheffield, Mappin Street, Sheffield S1 3JD, UK

⁴Department of Physics and Astronomy, University of Sheffield, Hounsfield Road, Sheffield, S3 7RH, UK

⁵Department of Physics, University of Cambridge, Cavendish Laboratory, 19 JJ Thomson Avenue, Cambridge CB3 0HE, UK.

⁶Departament de Física Aplicada, Universitat d'Alacant, E-03080 Alacant, Spain

⁷Departamento de Física - Centro de Investigación en Óptica y Nanofísica, Regional Campus of International Excellence “Campus Mare Nostrum”, Universidad de Murcia, E-30100 Murcia, Spain

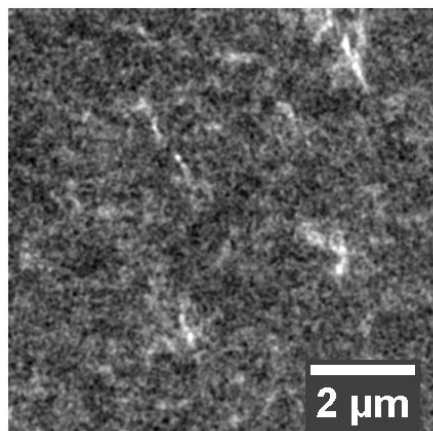
⁸FEI Company, Vlastimila Pecha 1282/12, 627 00 Brno, Czech Republic

⁹Laboratories for Electron Microscopy and Image Analysis, ISI AS CR, v.v.i. Královopolská 147, 612 64 Brno, Czech Republic

Correspondence to: Maurizio Dapor (E-mail: dapor@ectstar.eu)

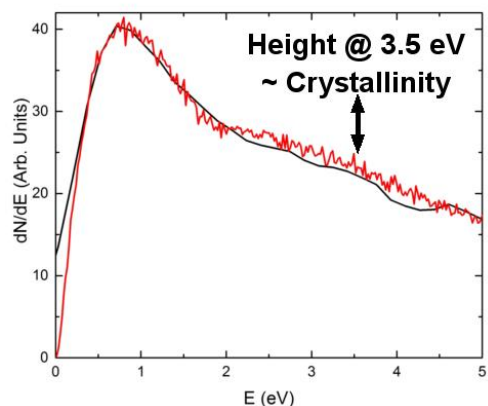
Additional Supporting Information may be found in the online version of this article.

ABSTRACT



P3HT

Secondary
electron spectrum
↔
Measure/model



The nano-scale dispersion of ordered/disordered phases in semi-crystalline polymers can strongly influence their performance e.g. in terms of mechanical properties and/or electronic properties. However, to reveal the latter in scanning electron microscopy (SEM) often requires invasive sample preparation (etching of amorphous phase), because SEM usually exploits topographical contrast or yield differences between different materials. However, for pure carbon materials the secondary spectra were shown to differ substantially with increased order/disorder. The aim here is to gain an understanding of the shape of secondary electron spectrum (SES) of a widely used semi-crystalline polymer regioregular poly(3-hexylthiophene-2,5-diyl), commonly known as P3HT, and its links to the underlying secondary electron emission mechanisms so SES can be exploited for the mapping the nano-morphology. The comparison of simulated and experimental SES shows an excellent agreement, revealing a peak (at about 0.8eV) followed by a broad shoulder (between 2eV and 4.5eV) with respective relative intensities reflecting order/disorder.

INTRODUCTION

Although a close relationship between Secondary electron (SE) emission spectra shape and materials properties was first observed 45 years ago[1] on carbon fibres, spectroscopy of

polymers is a field in its infancy as the origin of spectral features is complex, and could be influenced by orientation of molecules[1,2]. Nevertheless, the variations in emission spectrum have been applied to successfully monitor variations in morphology[3] in terms of chemical composition in the area of organic electronics[4] and the wide application to other carbon, nitrogen and oxygen containing nanostructured materials was predicted[5,6]. Although the SEM images in the above works have demonstrated high chemical sensitivity only the knowledge of the origin of spectral features is expected to take electron spectroscopy in the SEM out of its infancy and transform it to a widely used analytical tool for polymers.

Research, so far, has concentrated on the SE and total (*i.e.* SE plus backscattered electrons) yields, which are certainly important and useful when polymer surfaces are inspected using low primary beam energies, E_0 , (e.g. < 2 keV). In this condition links between SE yield and electronic structure were observed. For instance, it was reported[7] that materials with a high proportion of π -electrons emit a smaller number of SE than those with a smaller fraction of π electrons, and therefore appear darker in an SEM image. Furthermore, the primary beam voltage at which charge balance is established at the polymer surface, appears to be coupled to the number of valence electrons in the monomer as reported in[8], or to the number of valence electrons per molecular weight[9]. While such models for the SE emission yield can describe general trends reasonably well, the transport of internal SE towards the surface is very sensitive to the specific configuration of the polymer of interest, and its structural disorder[10]. The latter is likely to be the reason for differences in primary beam energies needed for charge balance even for polymers with nearly the same chemical composition[10]. Some evidence for this was seen in

SE images of P3HT films[4]. P3HT is a semiconducting polymer with varying degrees of disorder depending on processing conditions and is widely utilized in organic electronics[11–13]. Much of this paper is devoted to the detailed investigation of electrons emitted as result of low energy electron impact ($E_0= 200$ eV), investigating the role of disorder on the shape of the SE emission spectrum using Monte Carlo simulations, as well as experimental SE emission spectra with the aim to enable molecular mapping via energy filtered SEM.

Although Monte Carlo Calculation of Secondary Electron Emission from Organic Compounds were previously carried out[14] this was focused on the SE yields of polymers, and not on the shape of the SE emission spectra. Little work has been carried out in the area of SE emission spectra shapes, except for that of graphite and other allotrope forms of carbon[1,15], where multiple peaks have been observed. Some of these were explained as a result of the final density of empty states, with emission peaks correlating with structure in the material conduction band[1,15]. Chemically and micro-structurally more complex materials such as photoresist also exhibits more than one peak[16].

Here we investigate the origin of the SE spectrum measured from the semi-crystalline polymer, regioregular poly(3-hexylthiophene-2,5-diyl) (P3HT). The band structure of empty states in P3HT is complex and is not well understood in comparison to that of graphite, for example[17]. Furthermore, the band structure known to be strongly dependent on the sample processing and history, and aspects such as localized molecular ordering[18]. As such, we do not attempt to link the experimental SE spectrum of P3HT to the density of empty states, and instead take an alternative approach by modelling the SE spectrum to probe the origin of its shape.

Optical measurements on thick P3HT films suggest that the shapes of both the imaginary and the real parts of the dielectric function[19], and hence of the energy loss function (ELF), are influenced by the local order. In general, the ELF of the P3HT is characterized by the presence of two peaks. One peak is located at about 2.6 eV and relates to the π to π^* transition[20], which we call here for short π peak and is of high interest as it is in the energy range for optical absorption. The π peak height and its exact position in the ELF depend on ordering[20]. The second peak is the bulk plasmon peak resulting from collective oscillations of σ and π electrons[21] (henceforth called the $\pi+\sigma$ peak). Its position varies in different reports[22–24] ranging from 21.5 eV [23] to 23.4 eV[24].

In the present work we have derived the ELF from Electron Energy Loss Spectra (EELS) and use it as input parameter for a Monte Carlo modelling of SE spectra shapes of a low order P3HT sample.

Local order is not the only P3HT characteristic that influences the shape of SE spectra. Very important parameters that should be carefully considered, since they influence the SE emission, are the electron affinity χ of the material, *i.e.* the potential barrier between the vacuum level and the minimum of the conduction band (lowest unoccupied molecular orbital, LUMO), and the energy gap E_{gap} between the minimum of the conduction band (LUMO) and the maximum of the valence band (highest occupied molecular orbital, HOMO). The electron affinity truncates the lower end of the SE spectrum[25]. In fact, electrons approaching the surface from within the bulk see this potential barrier and must have energy larger than the electron affinity to overcome it. As a consequence, many electrons reaching the surface with low energy are not able to emerge from the surface[25,26]. The measured value of χ for a P3HT layer from the

analysis of the dark current-voltage characteristics of P3HT/n-type crystalline silicon solar cells is, according to Nolasco *et al.*, 3.2eV[27]. These authors also report results from other laboratories, which provided higher values of the P3HT electron affinity, up to 3.5eV[27]. Mallajosyula *et al.* on the other hand, measured the slightly smaller value of 3.13eV[28]. Actually, the value of the electron affinity can be strongly modified by the sample treatments and history. Air exposure can modify the sample electron affinity due to the oxygen and carbon contamination of the surface. Furthermore, unwanted sample doping can also be responsible of changes in this potential barrier. Last but not least, the ordering of the sample also influences the value of the electron affinity. Kanai *et al.* reported smaller values of the electron affinity of regioregular P3HT deposited on Si, 2.1eV for an as spin-cast P3HT sample (with low levels of crystallinity) and 2.3eV for a P3HT sample annealed at 170 °C to encourage further crystalline aggregation[29].

Also the band gap E_{gap} between the bottom of the conduction band and the top of the valence band of P3HT reported in the experimental literature covers a quite wide range of values. Kroon *et al.* reports the value of 1.9eV[30]. According to Nolasco *et al.* it ranges from 1.7 to 2.1 eV[27], while it ranges from 2.4eV to 2.6eV according to Kanai *et al.* (2.4eV: sample annealed at 170°, 2.6eV: as cast sample)[29].

Recent experimental evidences have been published demonstrating that electron mobility is also influenced by trapping phenomena[31,32]. For the case of P3HT, Armbruster *et al.* measured the dominant trap depth and provided the value of 130meV[31], while Schafferhans *et al.* reported the value of 105meV[32].

Electron-phonon interaction influences the low energy electron mobility in the solids as well. The electron-phonon cross section depends on the static dielectric constant ϵ_0 and on the high frequency dielectric constant ϵ_∞ . According to Singh *et al.* $\epsilon_0=30.3$ at room temperature, while $\epsilon_\infty=3.6$ [33].

In what follows, Monte Carlo simulations are presented in order to establish the influence of all the physical quantities described above on the shape of the SE energy distribution of a regioregular P3HT sample with low levels of crystalline aggregation.

The semi-classical approach (“trajectory+collision”) was assumed in this work. The use of such an approach (rather than a “wave function” method) could be questionable for low energy electrons. However, previous studies had shown that the use of the “trajectory+collision” approach for elastic collisions is a good approximation to quite low electron energies ($\approx 10\text{eV}$)[34], whereas for inelastic collisions that approximation is valid in the absence of short-range order and when the electron wavelength is similar or smaller than the average distance between nearest neighbour scatterers[35]. As both situations hold in our simulation, its results can be considered suitable

When comparing simulated and experimental spectra the influence of the spectrometer characteristics on the spectra shape cannot be ignored. For example, it was observed that the low energy region is particularly affected by differences in take off angle and spectrometer transfer characteristic[16]. Therefore, through the detailed Monte Carlo simulation, here we also investigate the effect of the spectrometer on the shape of the SE spectrum. We find that for our particular spectrometer setup the shape of the spectrum strongly depends on the working distance and that the same effect can be replicated in the model spectra by introducing a filtering depth D , which describes the thickness of a surface layer that does not contribute to the spectrum.

EXPERIMENTAL

P3HT film preparation

P3HT was purchased from Ossila Ltd. (type M107, $M_n = 15600$, $RR = 93.6\%$). Silicon substrates purchased from Ossila Ltd. were cleaned and rinsed in isopropanol and dried with a nitrogen gun.

For P3HT samples described as 'lower order', the dry polymer was dissolved in chloroform at a concentration of 25mg/ml and left on a hotplate overnight to ensure full dissolution. The P3HT solution was left to cool before being spin-cast on to the cleaned substrates at 2000rpm for 30s.

For P3HT samples described as 'higher order', the polymer was dissolved in dichlorobenzene and the solution aged for ~ 1 month under nitrogen atmosphere to increase the crystalline content of the solution[36]. The aged solution was then blade-coated on to a silicon substrate, as the higher viscosity of the aged solution made spin coating an ineffective deposition method.

EELS data collection and determination of ELF

EELS spectra were acquired on the JEOL R005 TEM using a Gatan Tridium detector with an accelerating voltage of 300kV and a dispersion of 0.05eV/pixel. The collection semi-angle was measured to be 0.33 mrad, while the convergence semi- angle was 7.83 mrad.

The beam current (which determines the dose) was chosen empirically; it was tuned by changing the extraction voltage of the microscope's cold FEG source to a value where the relevant plasmon peaks in the low loss EELS spectra could be observed to stay for more than 5s. Spectra for analysis were then taken from a fresh area each time, with exposure time of 1 s, which gave a dose of 130-290 $e^- \text{nm}^{-2}$ – around the lower bound of dose used in similar studies of this kind[20]. The raw spectrum and the exact method to determine the ELF from the raw data is described in the supporting information. The latter also contains a comparison to other published ELF data for P3HT.

Data collection and conversion to SES

First experimental SE spectra were measured on a FEI Sirion FEGSEM with XL-30 column, following procedures detailed in [4,37]. Briefly, energy-selective detection of SE was performed by reducing the bias, B , on the deflector electrode in the microscope's through-lens detector assembly. This places a low-pass filter on the detected SE, with the detection cutoff energy, E_c , correlated to a given value of B [37]. SE spectra were measured by imaging the sample with a 200 eV or 700 eV primary beam at 3 mm working distance and beam current 8.7 pA, with immersion lens active. A stack of images was taken of a single area $\sim 25 \mu\text{m}^2$, sequentially increasing the deflector bias, B , in small steps (0-30 V in 0.5 V steps). Plotting the brightness change of this stack as a function of B (or E_c) gives an integrated spectrum, which was differentiated to give the presented SES.

Further spectra were also taken using a FEI Nova NanoSEM 450 with a similar column and detector assembly. The method for measuring SE spectra here was identical to that used with the FEI Sirion, although different working distances were employed as indicated, and 0.2 V steps were used between each image in the spectrum stack. The beam current used to measure SES was estimated to be ~ 10 pA.

Connections between ELS and SE

The energy lost by each electron of the primary beam (see the EEL spectrum) in inelastic collisions along their path, is utilized to excite and ionize the atoms of the target. When a ionizations occur, the secondary electrons generated (conventionally the electrons emerging from the inelastic collisions with lower energy) travel in the solid producing a cascade of further secondary electrons. The great majority of this avalanche of secondary electrons do not emerge from the surface. In fact many of them do not reach the surface; furthermore, many secondary electrons that do reach the surface have not enough energy to overcome the potential barrier between the vacuum level and the minimum of the conduction band (the so-called electron

affinity, or work function). The fraction of secondary electrons that reach the surface satisfying the conditions to emerge, contribute to the experimentally observed SE spectrum.

Kramers-Kronig Analysis

In order to obtain the ELF plural scattering needs to be removed first. We used the Fourier Log method, with a fitting range from 0 eV to 2.8eV. Kramers-Kronig Analysis was then carried out using measured convergence semi-angles (7.83 mrad) and collection semi-angle of 0.33 mrad, with 10 iterations. The required optical refractive index was used as fitting parameter in order to obtain the closest match possible to literature data (from optical measurements) e.g. $n=1.45$ for low order P3HT and $n=1.9$ for high order P3HT. With this method we also obtain as a result a film thickness, which is 115 nm and 91 nm, respectively which are both within our expectations of film thickness as measured by AFM.

Monte Carlo modeling method

From the electron energy loss spectrum to the dielectric function

The relationship between the single-scattering spectrum $S(W)$ and the Energy Loss Function $\text{Im}[-1/\varepsilon(W)]$ is given by [38–40]

$$S(W) = \frac{I_0 t}{\pi a_0 m v^2} \text{Im} \left[\frac{-1}{\varepsilon(W)} \right] \ln \left[1 + \left(\frac{\beta}{\theta_W} \right)^2 \right], \quad (1)$$

where I_0 is the zero-loss density, t is the sample thickness, a_0 is the Bohr radius, m is the electron mass, v is the incident electron velocity, β is the collection semi-angle, $\theta_W = \frac{W}{\gamma m v^2}$ is a characteristic scattering angle for energy loss W , and γ is the relativistic factor.

We collected EELS data from an as spin cast (low order) P3HT sample. After application of the Fourier-Log transformation for dealing with elastic peak and multiple scattering[38], and of the transformation described by Eq. (1), we obtained the ELF of P3HT. Gatan Digital Micrograph was used to extract the ELF from the raw EELS data according to Eq. (1).

In order to perform the numerical calculations, an analytical expression of the ELF is needed. We have obtained a best fit to the experimental ELF by means of a sum of Drude-Lorentz functions[41]. The values of the strength, energy, and width of each oscillator of the best fit function are reported in Table 1. The extension of the ELF out from the optical domain (for momentum transfer k higher than 0) was obtained using the Drude-Lorentz theory with the following dispersion law[42]:

$$W(k) = W(k = 0) + \alpha_{RPA} \frac{\hbar^2 k^2}{2m} \quad (2)$$

where $\alpha_{RPA} = \frac{6E_F}{5E_p}$, with E_F being the Fermi energy, E_p the plasmon energy and m the electron mass.

Using the ELF obtained in such a way, we calculated the differential inverse inelastic mean free path (DIIMFP) and the inelastic mean free path (IMFP) of the low order P3HT.

Monte Carlo method

If r is a random number uniformly distributed in the interval [0,1], every step length Δs of each electron traveling in the solid is calculated assuming the Poisson statistics, so that

$$\Delta s = -\lambda \ln r. \quad (3)$$

In this equation, λ is the electron mean free path given by $(N\sigma)^{-1}$, where N is the number of molecules per unit volume in the solid target and σ is the total cross section.

The total cross section includes all the scattering mechanisms involved, so that it can be expressed as the sum of all the cross sections of the interactions of the electrons with the target: in particular, σ_{el} is the elastic scattering cross section due to the interaction among the incident electron and the screened atomic nuclei, σ_{inel} is the inelastic scattering cross section due to the interaction among the incident electron and the target ones (it is directly related to the target ELF), σ_{ph} is the scattering cross section due to the electron–phonon interactions, and σ_{trap} is the scattering cross section due to the trapping phenomena. When dealing with insulating materials, trapping phenomena are due to the so called polaronic effect, *i.e.* to the creation of a quasi-particle constituted by slow electrons with the polarization field around them[43]. In the case of a semiconducting polymer such as P3HT, traps result from a range of phenomena[44]. Oxygen impurities in the polymer chain are believed to be the dominant form of trap site, significantly affecting charge mobility[45](even in films not directly exposed to air or oxygen[46]). Other trapping effects include the misalignment of energy levels in crystalline and amorphous phases of the material[18,29]which can trap charges at the crystalline-amorphous boundary[44]. In this work, trapping has been described including the values of the density and energy of the traps taken from the experimental literature for this specific material[32].

Therefore,

$$\sigma = \sigma_{el} + \sigma_{inel} + \sigma_{ph} + \sigma_{trap}. \quad (4)$$

More details about the present Monte Carlo strategy can be found in [47].

Note that the elastic scattering cross section was calculated by using the relativistic partial wave expansion method (Mott cross section). Electron-atom elastic scattering cross section (described by Mott theory) is a purely elastic phenomenon, where the total kinetic energy (incident electron kinetic

energy plus atom kinetic energy) is conserved. Details of the numerical procedure utilized for the present calculations of the Mott cross section can be found in Refs[48–54].

The inelastic scattering cross section due to electron-electron interaction was calculated within the Ritchie theory[55].

Electron-phonon interaction was described using the Fröhlich theory[56,57]. The creation and annihilation of phonons correspond to truly inelastic processes (even if they are sometimes called “quasi-elastic”, as the energy transfer is very small) in which the total kinetic energy (incident electron kinetic energy plus atom kinetic energy) is not conserved, as a part of it is exchanged with phonons. Experimentally, an energy loss less than 0.1 eV cannot be detected, so the interaction is considered in the realm of elastic collisions; but in a simulation we can perfectly discriminate any energy loss. Note that if, on the one hand, the interaction is a quasi-elastic electron-phonon one, the simulation code describes atomic motion by phonons and electrons as Bloch waves. If, on the other hand, the collision is strictly elastic, the program considers basically isolated atoms and plane waves. Therefore, our simulation approach clearly distinguishes between the two phenomena (both originating from the electron projectile interaction with the target nuclei).

The cross-section for evaluating the trapping phenomena was described according to the same equation originally proposed by Ganachaud and Mokrani in order to describe the polaronic effect in insulating materials[43], but with a different interpretation: as already noted above, the dominant trapping phenomena in P3HT result from oxygen-related impurities [45].

Once the step-length is defined, the elastic or inelastic nature of the scattering event, the polar angle for elastic scattering and the energy loss for inelastic scattering are all sampled, according to the usual Monte Carlo recipes, via random numbers from the relevant cumulative probabilities[47].

RESULTS AND DISCUSSION

Inelastic mean free path data for MC model as obtained from EELS

In Fig.1 the ELF $\text{Im}[-1/\varepsilon(W)]$ derived (using equation 1) from transmission EELS data at 300kV is presented together with a best fit to this ELF using a sum of Drude-Lorentz functions[41]. Two oscillators with plasmon energies $W_1=2.8\text{eV}$ (π) and $W_2=22.5\text{eV}$ ($\pi+\sigma$) are clearly visible in the picture. Both oscillator positions are consistent with other reported EELS data for regio-regular P3HT and seem therefore representative[19,23]. However, we note that differences in degree of crystalline order do effect the peak position of the first Drude-Lorentz component of $W_1=2.8\text{eV}$ [see supporting information Fig. S3], as well as the peak width.

We then used the sum of the Drude-Lorentz functions as input data in order to obtain values for the inelastic mean free path (IMFP) related to the electron-electron collisions, in the energy range probed by the EELS experiments. We also derived the real and imaginary parts of the dielectric function from this ELF fit, from which the optical band-gap of the film can be deduced as 2.2 eV (see Figure S2 in the supplementary information). Our results match those found in literature [17], confirming the accuracy of the Drude-Lorentz fit in Fig. 1.

Fig.2 shows the resulting IMFP for electrons with energies in the range just above the energy gap (E_{gap} , between the minimum of the LUMO level and the maximum of the HOMO level) up to energies of 2000 eV. The IMFP quickly increases as the electron energy decreases toward the value of E_{gap} . This means that the probability of inelastic scattering goes to zero when the energy of the incident electron approaches E_{gap} . The reason of such a behavior is that incident electrons with energy smaller than E_{gap} cannot promote electrons from the HOMO level to the LUMO level[58]. The remaining inelastic scattering mechanisms are electron-phonon interactions[59]. Hence the IMFP results in unrealistically large values when the latter interaction is not included in the model.

In Fig.3 the comparison between electron-electron and electron-phonon IMFP and IMFP as result of trapping and the overall resulting IMFP in low order P3HT is presented. As the probability of interaction

is proportional to the reciprocal of the IMFP, Fig.3 shows that (i) below 6eV the probability of electron-phonon interaction becomes higher than the probability of electron-electron interaction and (ii) when the probability of electron-electron interaction becomes equal to zero, below the energy of the band gap (2.2eV, see below), the probability of electron-phonon interaction is finite, increases as the energy decreases and thus strongly dominates the total IMFP, as trapping only plays a minor role. The total IMFP reaches its maximum value of 35 Å for electrons with energies between 2.7 eV and 6 eV and then steadily decreases with for electrons with higher energies. Note that the effects of the various inelastic scattering cross-sections on the energy losses are very different. While the electron-phonon excitation leads to an energy loss of 50meV, the electron-electron excitation leads to an energy loss of several eV, even below 6eV.

Simulated secondary electron emission spectrum shows π and $\pi+\sigma$ features

The Monte Carlo simulation of the energy distribution of the electrons emerging from the surface of low order P3HT is presented in Fig.4 for an incident electron energy $E_0 = 200$ eV. This E_0 was used as it is below the K-shell ionisation energy for carbon, thus preventing significant ionization damage during experimental spectra collection, as the latter was reported to be an important damage mechanism in polymers exposed to electron beam[60].

In Fig.4 both the SE peak at about 0.8 eV and the elastic peak (from zero-loss reflected electrons) at 200 eV are clearly visible in the spectrum (note that the zero of the energy scale is located at the vacuum level).

A zoom of Fig.4 in an energy range close to the elastic peak, presenting the backscattered electrons and, in particular, the peaks related to reflected electrons with plasmon losses, is presented in Fig.5. Both the π and the $\pi+\sigma$ (~ 2.8 eV and ~ 22.5 eV energy loss, respectively) peaks, already described when we discussed the ELF data, can be observed, albeit with peak energies slightly shifted from the plasmon loss

energies (due to the energy-dependent $\ln\left[1 + \left(\frac{\beta}{\theta_w}\right)^2\right]$ term in equation 1, which relates the EELS spectrum to the ELF [38]). The substantially stronger SE peak (0.8 eV) compared to the π and the $\pi+\sigma$ peaks from reflected electrons with plasmon losses is obvious. As the consequence SE imaging may be carried out at lower doses than low loss BSE imaging when a given signal to noise ratio of the image is required.

Therefore, it is worth to notice also the effects of the plasmon losses in the secondary electron spectrum, which lead to the shoulder appearing at 10-24 eV in Fig. 4. The implications of this feature will be discussed below.

This MC simulation was performed with the following values of the parameters: average phonon energy=0.05eV, $\epsilon_0=30.3$, $\epsilon_\infty=3.6$, trap depth=105meV, traps per unit length=0.01nm⁻¹, number of primary electrons=10⁷. We determined the value of the band gap using our EELS data, and found $E_{\text{gap}}=2.2\text{eV}$. According to Kanai *et al.* the sum of the band gap and the electron affinity of P3HT is 4.7 eV[29]. So, we used, for the electron affinity of our sample, the value of 2.5eV (between the value measured by Kanai *et al.* for an as cast sample of P3HT, *i.e.* 2.1eV, and that provided by Nolasco *et al.*, *i.e.* 3.2eV).

Hence the shoulder at ~20 eV in Fig. 4 can be explained as a result of the $\pi+\sigma$ plasmon interaction based on its peak location. The energy loss related to the π -peak in the ELF does not lead to a notable feature.

Note that the MC simulation collects all the emerging electrons without any distinction between backscattered electrons and SEs. This is exactly what the experiment allows to observe, since electrons are indistinguishable, even if it is quite clear that the great majority of SEs emerges with energies smaller than 50 eV, and the great majority of backscattered electrons emerges with energies higher than 50eV. For a recent discussion about the importance of simulating the trajectories of all the electrons (both backscattered and secondary) for a correct description of the spectrum, see Ref [61].

The shape of the experimental SES in the low energy range <5eV (measured from vacuum level) has similarity to UPS and depends on degree of crystallinity.

Our primary experimental SES were measured using a FEI Sirion SEM, a well-studied microscope with regards to its SE spectroscopy capabilities[4,26]. However, in order to separate material and spectrometer effects on the SES shape, we collected SES from different P3HT samples, as well as measuring SES from P3HT in an additional SEM (FEI Nova NanoSEM 450) and under different collection conditions. Figure 6a shows the spectra collected in different microscopes with similar detection schemes but some difference in electron optics. The SES as measured from different microscopes are similar: a peak followed by a long tail-off at the higher-energy side. A very similar shape can be observed in the He I UPS spectrum of P3HT (Supporting Information, Figure S5)[62].

To emphasise the effects the material has on the measured SE spectra, in Fig. 6b we present the SES from both a lower order regioregular P3HT sample as well as one with a higher degree of crystallinity (as demonstrated by UV-visible spectroscopy of the two P3HT samples, presented in the supporting information, Figure S6). It is observed that a peak at ~ 3.5 eV becomes far more defined in the SES of the highly-ordered sample, suggesting that crystalline regions of P3HT are strongly emissive at this energy. This is unsurprising; similar variation can be found in UPS spectra of P3HT samples processed with different levels of molecular ordering[63]. The effect may indicate a compelling potential application of SE spectroscopy to polymer samples, whereby SES and energy-filtered SE imaging may be used to probe for localised ordering in semi-crystalline materials. As previously reported at higher primary beam energies[4], we find that localised variations in ordering do appear with high contrast in energy-filtered SE images of P3HT at $E_0 = 200$ eV (see Fig. 6b inset, with further examples and a brief discussion in the Supporting Information, Figure S7). Features such as this are sparsely populated throughout the surface of the P3HT film, with size of a few hundred nm. The technique is thus a potentially powerful method of

mapping crystallinity in a P3HT sample. However, the nature of these features is beyond the scope of this paper and will be the focus of future work.

Working distance influences the shape of experimental SES and controls whether SE from the surface are suppressed.

In order to effectively compare experimental and simulated spectra, we must first consider the limitations of our SE spectrometer, and the effects these have on the nature of our experimentally-acquired SES. In particular, the collection efficiency of our SE detector is known to be a function of sample working distance and SE emission angles[64].

Hence, in Fig 6c we investigate the influence of the chosen working distance on the spectra shape for the NOVA. The data were collected using a primary beam energy of 700 eV, as for the 200 eV primary beam we find it difficult to obtain reliable data for working distances exceeding 3mm. We note that the spectrum shape for 200 eV and 700 eV and the same working distance is broadly similar, in that one low energy peak is followed by a second peak. The peak positions (indicated by vertical dashed lines in Fig. 6) are independent of the primary beam energy.

As can be seen in Fig. 6, the working distance has a much stronger influence on SES shape than the primary beam energy, and can alter the shape drastically from a clear two-peak distribution to a low energy peak and a shoulder. This implies a reduced collection efficiency when the working distance increases, with SE emitted at various energies affected differently.

Figure 7 shows the change of the detected signal for SE emitted within different energy ranges. Low energy SEs experience a high degree of collimation independently of emission angle[65] and thus are effectively collected by our SE detector at any working distance. In contrast higher energy SEs emitted at large emission angles require a strong extraction field to collect. The latter is weakened with increasing working distance. The overall effect is that SES collected at larger working distances (3mm and above) for both our instruments are dominated by low energy SEs.

Previously, a link between the energy of a detected SE and its depth of origin within the sample has been demonstrated for our instruments[64,66]. This effect is explained as a result of the momentum vector an internal SE requires to overcome the surface emission barrier of the sample. This surface barrier acts only to reduce the momentum component of an internal SE in the direction normal to the surface (p_{\perp}). We assume the barrier height, E_B , to be equal to the electron affinity of the sample, taken in this work as 2.5 eV in the case of P3HT.

The smallest momentum sufficient for escape is

$$p_{min} = \sqrt{2mE_B} \quad (5)$$

For the case of an internal SE with momentum normal to the surface (internal angle $\vartheta=0$). If the momentum is larger than p_{min} , the momentum vector of the internal SE may have a component tangential to the surface, p_{\parallel} and still escape the sample. However, if an internal SE of a given energy, $E_{SE(i)}$, is to be emitted, then the magnitude of p_{\parallel} , and therefore ϑ , are limited by the fact that p_{\perp} must be larger than p_{min} . In particular, internal SE with energy $E_{SE(i)}$ can only escape if their momentum vector has a direction for which its internal $\vartheta < \cos^{-1} \sqrt{E_B/E_{SE(i)}}$ [64]. This means higher energy SEs can be emitted with much larger angles (supporting information, Figure S8).

For our detection system it has been shown previously[64,67] that SE emitted with large external θ cannot be detected efficiently, and that this effect is exacerbated at larger working distances[64]. As a result, a significant fraction of SE that originate with larger $E_{SE(i)}$ (i.e. those with a large p_{\parallel} component) do not contribute to the detected spectrum.

Let us now compare two internal SE with the same overall momentum (larger than p_{min}). One has a small p_{\parallel} component and as such is detected in our system, and one has a large enough p_{\parallel} component such that its resulting external SE can not be detected. We further assume that both SE travelled over

the same length. As such the SE with the larger p_{\parallel} component would need to originate closer to the surface. As only the latter is not detected, SE that originated from close to the surface are under-represented in our measured spectrum in comparison to the spectrum obtained from modelling. To account for these limitations of our spectrometer in our simulations, we introduce a filtering depth parameter D to our simulations which indicates the depth from which SE emission is not adequately represented in the experimentally measured spectrum. When applying a filtering depth to our simulation, we consider only emitted SE that are generated at a depth below D .

Naturally D is not a fixed depth but strongly depends on the angular acceptance range of the detection system. The latter can be weakened by increasing the working distance as shown previously[64], which would result in enhanced effect and larger D , or indeed smaller D if the working distance is reduced. We should further note that D is not an exact correction – naturally, SE generated at the surface with low ϑ and p_{\perp} larger than p_{min} can be detected using our system. However, as a simple, effective method of reconciling our simulated and experimentally acquired spectra, we feel it is justified as a large fraction of SEs generated near the surface will not be detected due to the above considerations.

Importantly, inspection of Figures 6b and 8 confirm the effectiveness of introducing D as a parameter to our simulations: reducing the efficiency of our detection system through increasing the working distance has the same effect on the shape of the SE spectrum as introducing D to the model spectra (over the energy region investigated). In both Figures we see a reduction of the higher energy SE contribution to the spectrum. Figure 7 contains further confirmation for the above hypothesis. We note that only SE with kinetic energies larger than 1eV show a dependence on working distance. Such electrons are more likely to have a larger p_{\parallel} component, and will be more aggressively filtered out at larger working distances.

Comparison of experimentally observed SES shape to simulated SES points to strong role of bandgap.

The modelled SES is presented in Fig. 9, which also contains our experimental SES (Sirion, working distance= 3mm) for comparison. Note that the data presented in Fig.9 were obtained with $D=2.5\text{nm}$.

The Monte Carlo simulated SES shows a peak at very low energy (about 0.8eV above the vacuum level) followed by a smooth decrease of the spectrum and a second very broad shoulder, located from 2 eV to 4.5 eV above the vacuum level, very similar to that experimentally observed. The reason of this shape is that, as the energy of the SEs decreases below the band-gap plus electron affinity SEs are less effective in exciting electrons from the valence band to the conduction band, as the probability of electron-electron scattering quickly decreases (while the total IMFP increases; see Fig. 3). As a consequence, more electrons can emerge, when an important mechanism of energy loss is less effective. Based on this explanation any changes in bandgap would be expected in a change of the broader higher energy feature located from 2 eV to 4.5 eV above the vacuum level. That this is indeed the case was already shown in Fig 6b, where this features becomes more pronounced in the material with a higher degree in crystallinity that has a smaller bandgap as was shown in [Supporting information, Figure S4]. The increased emission in this energy range is responsible for an overall higher SE yield. Therefore, our observation of this features directly corroborates the finding of a strong role of bandgap on the SE emission yield in semiconducting carbon materials[58].

If the second peak which seems to be related to the bandgap can be experimentally detected depends strongly on the exact experimental conditions, in particular on the working distance. For working distances of 2mm and 3mm the double peak is visible but a further increase in working distance emphasizes the low energy peak so strongly that it becomes hard to locate the broader higher energy peak. However, SES collected at larger working distance increasingly suppress SE emitted from the surface. Such SES therefore reflect the bulk material rather than the surface, thus reducing any effects of surface contamination[26].

Future developments

We note that this work was performed at $E_0 = 200$ eV, below the energy used for conventional low-voltage SEM imaging. By measuring SES at higher E_0 , further interactions such as core-electron emission are possible, which will bring additional complexity to the measured SE spectrum. This is evidenced by comparison of the SES of P3HT in Figure 6a (measured at 200 eV), with those shown in Figure 6c (700 eV) and those reported in[4] (1 keV).

Furthermore, the resolution of our experimental SES is limited to ~ 0.2 eV. As such, finer features may be suppressed or not resolved in our experimental data. This may be due in part to the aging nature of the FEI Sirion SEM which was used to record our primary spectra. Achieving a thorough verification and optimization of SE spectroscopy methods (similar to that already achieved on the FEI Sirion) is possible on new SEM models. For example, a full verification of the FEI Nova used to measure some SES in Figure 6 should allow for improvement in this regard.

As the energy loss function describes the probability of energy loss in different scattering events, its accurate calculation is very important. In this work we have determined it with great accuracy, starting from EELS data acquired in the range of energy losses from 0 to 90 eV (see Fig. 1). Higher energy excitations (from atomic levels below the valence band), though much less probable than plasmon excitations, can, when they occur, make an important contribution to the SE cascade. Though not relevant to the present study of one polymer, such higher energy excitations could be significant in explaining differences in total SE yield in different polymers (*e.g.* whether or not they contain sulfur). We plan to investigate the effects of these high energy excitations by using the dielectric formalism together with the Mermin energy loss function - generalized oscillator strength (MELF-GOS) method[68].

Since we are taking into account of momentum transfer as well as energy transfer, the threshold energy E_t for inelastic electron excitation (measured from the bottom of the conduction band) is typically higher than the energy gap, with $E_t = (1 + \alpha) E_{gap}$ [59]. In general, α depends on the details of the electronic band structure. The energy band structure of the target above the vacuum energy level becomes important when electron energy is very low, and this property is difficult to handle using the Monte Carlo method. Hence, another future development of the present study will be dedicated to the effect of changes in the band structure as a result of variations in polymer morphology.

The present work was devoted to the simulation of the shape of the energy spectrum, which is in very good agreement with the experimental one (Fig. 9). In order to simulate also the yield, we plan to consider, as a further development of the present work, the whole spectra of both the reflected and transmitted electrons and to integrate them over energy. In fact, unless significant numbers of electrons stay trapped in the specimen, such an integration should correspond to the incident flux.

CONCLUSIONS

We compared Monte Carlo simulated results with experimental data of SE spectra of P3HT for a primary electron beam energy of 200 eV. Such a comparison allowed us to evaluate the minimum depth of provenience of the emitted SEs in our experiment, which we find depends on the chosen working distance. The simulation was also used to provide an interpretation of the shape of the SE spectrum, *i.e.* a peak (located at about 0.8eV) followed by a broad shoulder (between 2eV and 4.5eV).

Based on the above knowledge about the SES spectrum, we can explain the strong nano-scale image contrast in energy filtered SEM images of semi-polycrystalline P3HT to result from local variations in bandgap, caused by differences in crystallinity. Hence, we believe that SES spectra potential as a novel characterisation tool for semi-crystalline polymers.

ACKNOWLEDGEMENTS

The authors wish to thank Professor A. M Donald, University of Cambridge, for discussions and express their warm gratitude to Professor A. Howie, University of Cambridge, for the stimulating comments and helpful suggestions with regards to future developments. MD acknowledges the support of the Leverhulme Trust through the Visiting Professorship (VP1-2014-011) that made this project possible. IA and RGM thank partial financial support by the Spanish Ministerio de Economía y Competitividad (Project FIS2014-58849-P) and the Murcia Regional Agency of Science and Technology (project 19907/GERM/15). CR thanks EPSRC for funding under grant EP/N008065/1.

REFERENCES AND NOTES

- [1] R.F. Willis, B. Fitton, D.K. Skinner, Study of carbon-fiber surfaces using Auger and secondary electron emission spectroscopy, *J. Appl. Phys.* 43 (1972) 4412–4419. doi:10.1063/1.1660936.
- [2] C. Rodenburg, R.C. Masters, D.G. Lidzey, M. Uncovsky, T. Vystavěl, F. Mika, SECONDARY ELECTRON SPECTROSCOPY AND ENERGY SELECTIVE IMAGING FOR THE ENGINEERING OF CARBON BASED MATERIALS, in: *Proc. Recent Trends Charg. Part. Opt. Surf. Phys. Instrum.*, Brno, 2016: pp. 58–59.
- [3] R. Rasch, A. Stricher, R.W. Truss, Energy filtered low voltage “in lens detector” SEM and XPS of natural fiber surfaces, *J. Appl. Polym. Sci.* 131 (2014) 39572. doi:10.1002/app.39572.
- [4] R.C. Masters, A.J. Pearson, T.S. Glen, F.-C. Sasam, L. Li, M. Dapor, A.M. Donald, D.G. Lidzey, C. Rodenburg, Sub-nanometre resolution imaging of polymer–fullerene photovoltaic blends using energy-filtered scanning electron microscopy, *Nat. Commun.* 6 (2015) 6928. doi:10.1038/ncomms7928.
- [5] H. Jaksch, Imaging exotic nano structured compositions , polymers and protein with Low Loss BSE electrons in a Field Emission SEM, in: *Proc. Microsc. Conf. 2009, Graz, 2009*: pp. 289–290. doi:10.3217/978-3-85125-062-6-143.
- [6] H. Jaksch, LL-BSE electron contrast from Hybridization & Band Gaps in FE-SEM, in: *Proc. Eur. Microsc. Conf. 2012, Manchester, 2012*.
- [7] Y. Kishimoto, T. Ohshima, M. Hashimoto, T. Hayashi, A consideration of secondary electron emission from organic solids, *J. Appl. Polym. Sci.* 39 (1990) 2055–2066. doi:10.1002/app.1990.070391003.
- [8] E.A. Burke, Secondary Emission from Polymers, *IEEE Trans. Nucl. Sci.* 27 (1980) 1759–1764. doi:10.1109/TNS.1980.4331102.
- [9] J. Butler, D.C. Joy, G. Bradley, S. Krause, Low-voltage scanning electron microscopy of polymers, *Polymer (Guildf)*. 36 (1995) 1781–1790. [http://dx.doi.org/10.1016/0032-3861\(95\)90924-Q](http://dx.doi.org/10.1016/0032-3861(95)90924-Q)

(accessed October 13, 2013).

- [10] J. Cazaux, A new model of dependence of secondary electron emission yield on primary electron energy for application to polymers, *J. Phys. D. Appl. Phys.* 38 (2005) 2433–2441. doi:10.1088/0022-3727/38/14/020.
- [11] J. You, L. Dou, K. Yoshimura, T. Kato, K. Ohya, T. Moriarty, K. Emery, C.-C. Chen, J. Gao, G. Li, Y. Yang, A polymer tandem solar cell with 10.6% power conversion efficiency., *Nat. Commun.* 4 (2013) 1446. doi:10.1038/ncomms2411.
- [12] M.P. Bhatt, H.D. Magurudeniya, E.A. Rainbolt, P. Huang, D.S. Dissanayake, M.C. Biewer, M.C. Stefan, Poly(3-Hexylthiophene) Nanostructured Materials for Organic Electronics Applications, *J. Nanosci. Nanotechnol.* 14 (2014) 1033–1050. doi:10.1166/jnn.2014.8892.
- [13] M. Brinkmann, L. Hartmann, L. Biniek, K. Tremel, N. Kayunkid, Orienting semi-conducting π -conjugated polymers, *Macromol. Rapid Commun.* 35 (2014) 9–26. doi:10.1002/marc.201300712.
- [14] M. Yasuda, T. Nobuo, H. Kawata, A monte carlo calculation of secondary electron emission from organic compounds, *Japanese J. Appl. Physics, Part 1 Regul. Pap. Short Notes Rev. Pap.* 43 (2004) 4004–4008. doi:10.1143/JJAP.43.4004.
- [15] J. Ferrón, R.A. Vidal, N. Bajales, L. Cristina, R.A. Baragiola, Role of HOPG density of empty electronic states above vacuum on electron emission spectra induced by ions and UV photons, *Surf. Sci.* 622 (2014) 83–86. doi:10.1016/j.susc.2013.12.010.
- [16] S.P. Mulapudi, *Fundamental studies of X-ray and Secondary Electron Spectroscopy*, University of Knoxville, Tennessee, 2004.
- [17] J.A. Alexander, F.J. Scheltens, L.F. Drummy, M.F. Durstock, J.B. Gilchrist, S. Heutz, D.W. McComb, Measurement of optical properties in organic photovoltaic materials using monochromated electron energy-loss spectroscopy, *J. Mater. Chem. A.* 4 (2016) 13636–13645. doi:10.1039/C6TA06201F.
- [18] L.G. Kaake, P.F. Barbara, X.Y. Zhu, Intrinsic charge trapping in organic and polymeric semiconductors: A physical chemistry perspective, *J. Phys. Chem. Lett.* 1 (2010) 628–635. doi:10.1021/jz9002857.
- [19] S. Engmann, V. Turkovic, P. Denner, H. Hoppe, G. Gobsch, Optical order of the polymer phase within polymer/fullerene blend films, *J. Polym. Sci. Part B Polym. Phys.* 50 (2012) 1363–1373. doi:10.1002/polb.23131.
- [20] C. Guo, F.I. Allen, Y. Lee, T.P. Le, C. Song, J. Ciston, A.M. Minor, E.D. Gomez, Probing Local Electronic Transitions in Organic Semiconductors through Energy-Loss Spectrum Imaging in the Transmission Electron Microscope, *Adv. Funct. Mater.* 25 (2015) 6071–6076. doi:10.1002/adfm.201502090.
- [21] M.K. Barbarez, D.K.D. Gupta, D. Hayward, On the mechanisms of characteristic electron energy loss spectra of polymers, *J. Phys. D. Appl. Phys.* 10 (1977) 1789–1800. doi:10.1088/0022-3727/10/13/015.
- [22] A.A. Herzog, L.J. Richter, I.M. Anderson, 3D Nanoscale Characterization of Thin-Film Organic Photovoltaic Device Structures via Spectroscopic Contrast in the TEM, *J. Phys. Chem. C.* 114 (2010) 17501–17508. doi:10.1021/jp105883p.
- [23] M. Pfannmöller, H. Flügge, G. Benner, I. Wacker, C. Sommer, M. Hanselmann, S. Schmale, H. Schmidt, F. a Hamprecht, T. Rabe, W. Kowalsky, R.R. Schröder, Visualizing a homogeneous blend

- in bulk heterojunction polymer solar cells by analytical electron microscopy., *Nano Lett.* 11 (2011) 3099–3107. doi:10.1021/nl201078t.
- [24] J. A. Amonoo, E. Glynos, X.C. Chen, P.F. Green, An Alternative Processing Strategy for Organic Photovoltaic Devices Using a Supercritical Fluid, *J. Phys. Chem. C.* 116 (2012) 20708–20716. doi:10.1021/jp304976x.
- [25] M. Dapor, B.J. Inkson, C. Rodenburg, J.M. Rodenburg, A comprehensive Monte Carlo calculation of dopant contrast in secondary-electron imaging, *EPL (Europhysics Lett.)* 82 (2008) 30006. doi:10.1209/0295-5075/82/30006.
- [26] C. Rodenburg, M. a E. Jepsen, E.G.T. Bosch, M. Dapor, Energy selective scanning electron microscopy to reduce the effect of contamination layers on scanning electron microscope dopant mapping., *Ultramicroscopy.* 110 (2010) 1185–1191. doi:10.1016/j.ultramic.2010.04.008.
- [27] J.C. Nolasco, R. Cabré, J. Ferré-Borrull, L.F. Marsal, M. Estrada, J. Pallarès, Extraction of poly (3-hexylthiophene) (P3HT) properties from dark current voltage characteristics in a P3HT/n-crystalline-silicon solar cell, *J. Appl. Phys.* 107 (2010) 44505. doi:10.1063/1.3296294.
- [28] A.T. Mallajosyula, S.S.K. Iyer, B. Mazhari, Conduction properties of carbon nanotubes in P3HT:SWNT bulk heterojunction solar cells, in: 2008 33rd IEEE Photovoltaic Spec. Conf., IEEE, 2008: pp. 1–6. doi:10.1109/PVSC.2008.4922722.
- [29] K. Kanai, T. Miyazaki, H. Suzuki, M. Inaba, Y. Ouchi, K. Seki, Effect of annealing on the electronic structure of poly(3-hexylthiophene) thin film., *Phys. Chem. Chem. Phys.* 12 (2010) 273–282. doi:10.1039/b914100f.
- [30] R. Kroon, M. Lenes, J.C. Hummelen, P.W.M. Blom, B. de Boer, Small Bandgap Polymers for Organic Solar Cells (Polymer Material Development in the Last 5 Years), *Polym. Rev.* 48 (2008) 531–582. doi:10.1080/15583720802231833.
- [31] O. Armbruster, C. Lungenschmied, S. Bauer, Investigation of trap states and mobility in organic semiconductor devices by dielectric spectroscopy: Oxygen-doped P3HT:PCBM solar cells, *Phys. Rev. B.* 86 (2012) 235201. doi:10.1103/PhysRevB.86.235201.
- [32] J. Schafferhans, A. Baumann, A. Wagenpfahl, C. Deibel, V. Dyakonov, Oxygen doping of P3HT:PCBM blends: Influence on trap states, charge carrier mobility and solar cell performance, *Org. Electron.* 11 (2010) 1693–1700. doi:10.1016/j.orgel.2010.07.016.
- [33] R. Singh, R.K. Singh, J. Kumar, R. Kant, V. Kumar, The origin of DC electrical conduction and dielectric relaxation in pristine and doped poly(3-hexylthiophene) films, *J. Polym. Sci. Part B Polym. Phys.* 48 (2010) 1047–1053. doi:10.1002/polb.21994.
- [34] D. Liljequist, A study of errors in trajectory simulation with relevance for 0.2–50eV electrons in liquid water, *Radiat. Phys. Chem.* 77 (2008) 835–853. doi:10.1016/j.radphyschem.2008.03.004.
- [35] D. Liljequist, Coherent elastic scattering trajectory simulation, *Nucl. Instruments Methods Phys. Res. Sect. B Beam Interact. with Mater. Atoms.* 275 (2012) 79–85. doi:10.1016/j.nimb.2011.12.063.
- [36] U. Bielecka, P. Lutsyk, K. Janus, J. Sworakowski, W. Bartkowiak, Effect of solution aging on morphology and electrical characteristics of regioregular P3HT FETs fabricated by spin coating and spray coating, *Org. Electron. Physics, Mater. Appl.* 12 (2011) 1768–1776. doi:10.1016/j.orgel.2011.06.027.
- [37] P. Kazemian, S. a M. Mentink, C. Rodenburg, C.J. Humphreys, Quantitative secondary electron

- energy filtering in a scanning electron microscope and its applications., *Ultramicroscopy*. 107 (2007) 140–150. doi:10.1016/j.ultramic.2006.06.003.
- [38] R.F. Egerton, *Electron Energy-Loss Spectroscopy in the Electron Microscope*, Springer US, Boston, MA, 2011. doi:10.1007/978-1-4419-9583-4.
- [39] M. Stöger-Pollach, A. Laister, P. Schattschneider, Treating retardation effects in valence EELS spectra for Kramers–Kronig analysis, *Ultramicroscopy*. 108 (2008) 439–444. doi:10.1016/j.ultramic.2007.07.003.
- [40] D.T.L. Alexander, P.A. Crozier, J.R. Anderson, Brown carbon spheres in East Asian outflow and their optical properties., *Science*. 321 (2008) 833–6. doi:10.1126/science.1155296.
- [41] R.H. Ritchie, A. Howie, Electron excitation and the optical potential in electron microscopy, *Philos. Mag.* 36 (1977) 463–481. doi:10.1080/14786437708244948.
- [42] M. Dapor, I. Abril, P. de Vera, R. Garcia-Molina, Simulation of the secondary electrons energy deposition produced by proton beams in PMMA: influence of the target electronic excitation description, *Eur. Phys. J. D*. 69 (2015) 165. doi:10.1140/epjd/e2015-60123-7.
- [43] J.P. Ganachaud, A. Mokrani, Theoretical study of the secondary electron emission of insulating targets, *Surf. Sci.* 334 (1995) 329–341. doi:10.1016/0039-6028(95)00474-2.
- [44] J. Schafferhans, Investigation of defect states in organic semiconductors : Towards long term stable materials for organic photovoltaics, Julius-Maximilians-Universitaet Wuerzburg, 2011. <http://opus.bibliothek.uni-wuerzburg.de/volltexte/2011/5766/>.
- [45] J. Schafferhans, A. Baumann, C. Deibel, V. Dyakonov, Trap distribution and the impact of oxygen-induced traps on the charge transport in poly(3-hexylthiophene), *Appl. Phys. Lett.* 93 (2008). doi:10.1063/1.2978237.
- [46] C.H. Peters, I.T. Sachs-Quintana, W.R. Mateker, T. Heumueller, J. Rivnay, R. Noriega, Z.M. Beiley, E.T. Hoke, A. Salleo, M.D. McGehee, The mechanism of burn-in loss in a high efficiency polymer solar cell, *Adv. Mater.* 24 (2012) 663–668. doi:10.1002/adma.201103010.
- [47] M. Dapor, *Transport of Energetic Electrons in Solids*, Springer, Berlin, 2014.
- [48] N.F. Mott, The Scattering of Fast Electrons by Atomic Nuclei, *Proc. R. Soc. A Math. Phys. Eng. Sci.* 124 (1929) 425–442. doi:10.1098/rspa.1929.0127.
- [49] S.-R. Lin, N. Sherman, J.K. Percus, Elastic scattering of relativistic electrons by screened atomic nuclei, *Nucl. Phys.* 45 (1963) 492–504. doi:10.1016/0029-5582(63)90824-1.
- [50] P.J. Bunyan, J.L. Schonfelder, Polarization by mercury of 100 to 2000 eV electrons, *Proc. Phys. Soc.* 85 (1965) 455–462. doi:10.1088/0370-1328/85/3/306.
- [51] F. Salvat, R. Mayol, Elastic scattering of electrons and positrons by atoms. Schrödinger and Dirac partial wave analysis, *Comput. Phys. Commun.* 74 (1993) 358–374. doi:10.1016/0010-4655(93)90019-9.
- [52] M. Dapor, Elastic scattering calculations for electrons and positrons in solid targets, *J. Appl. Phys.* 79 (1996) 8406–8411. doi:10.1063/1.362514.
- [53] M. Dapor, *Electron-Beam Interactions with Solids*, Springer, Berlin, 2003.
- [54] A. Jablonski, F. Salvat, C.J. Powell, Comparison of Electron Elastic-Scattering Cross Sections Calculated from Two Commonly Used Atomic Potentials, *J. Phys. Chem. Ref. Data*. 33 (2004) 409–451. doi:10.1063/1.1595653.
- [55] R.H. Ritchie, Plasma Losses by Fast Electrons in Thin Films, *Phys. Rev.* 106 (1957) 874–881.

- doi:10.1103/PhysRev.106.874.
- [56] H. Fröhlich, Electrons in lattice fields, *Adv. Phys.* 3 (1954) 325–361. doi:10.1080/00018735400101213.
- [57] J. Llacer, E.L. Garwin, Electron-phonon interaction in alkali halides. I. The transport of secondary electrons with energies between 0.25 and 7.5 eV, *J. Appl. Phys.* 40 (1969) 2766–2775. doi:10.1063/1.1658075.
- [58] N.E. Nickles, *The Role of Bandgap in the Secondary Electron Emission of Small Bandgap Semiconductors: Studies of Graphitic Carbon*, Utah State University, 2002.
- [59] A. Howie, Threshold energy effects in secondary electron emission, *Microsc. Microanal.* 6 (2000) 291–296. doi:10.1007/s100050010042.
- [60] R. Garcia-Molina, A. Gras-Marti, Analytical theory of electron-beam-induced damage in organic materials, *J. Appl. Phys.* 61 (1987) 3105–3107. doi:10.1063/1.337811.
- [61] M. Dapor, Role of the tail of high-energy secondary electrons in the Monte Carlo evaluation of the fraction of electrons backscattered from polymethylmethacrylate, *Appl. Surf. Sci.* 391 (2017) 3–11. doi:10.1016/j.apsusc.2015.12.043.
- [62] H. Wei, L. Scudiero, H. Eilers, Infrared and photoelectron spectroscopy study of vapor phase deposited poly (3-hexylthiophene), *Appl. Surf. Sci.* 255 (2009) 8593–8597. doi:10.1016/j.apsusc.2009.06.031.
- [63] Y.C. Kwan, UPS and XPS study of annealed and unannealed poly-3-hexyl-thiophene, 2011.
- [64] C. Schönjahn, R.F. Broom, C.J. Humphreys, a. Howie, S. a M. Mentink, Optimizing and quantifying dopant mapping using a scanning electron microscope with a through-the-lens detector, *Appl. Phys. Lett.* 83 (2003) 293–295. doi:10.1063/1.1592302.
- [65] A. Khurshheed, *Scanning Electron Microscope Optics and Spectrometers*, World Scientific, Singapore, 2011.
- [66] T.H.P. Chang, W.C. Nixon, Electron beam induced potential contrast on unbiased planar transistors, *Solid. State. Electron.* 10 (1967) 701–704. doi:10.1016/0038-1101(67)90099-8.
- [67] C. Rodenburg, M. a E. Jepson, B.J. Inkson, E.G.T. Bosch, C.J. Humphreys, Energy filtered scanning electron microscopy: applications to characterisation of semiconductors, *J. Phys. Conf. Ser.* 241 (2010) 12074. doi:10.1088/1742-6596/241/1/012074.
- [68] I. Abril, R. Garcia-Molina, C.D. Denton, F.J. Pérez-Pérez, N.R. Arista, Dielectric description of wakes and stopping powers in solids, *Phys. Rev. A.* 58 (1998) 357–366. doi:10.1103/PhysRevA.58.357.

Figures

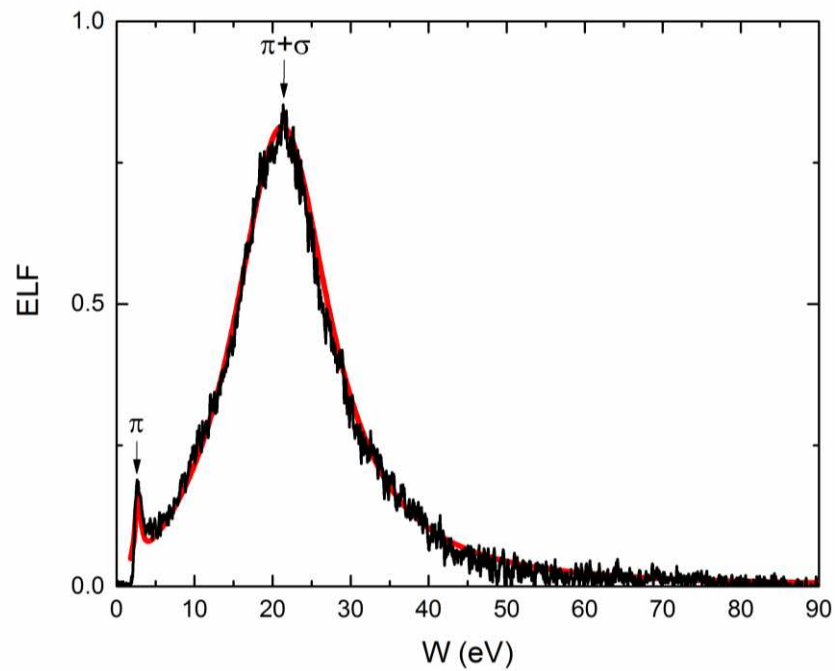


Fig.1. (Color online) Energy Loss Function (ELF) of the low order P3HT as a function of the energy loss W . Black line: experimental data, acquired with primary beam energy of 300kV. Red line: Sum of Drude-Lorentz functions (best fit of the ELF experimental data). Two oscillators located at $W=2.8\text{eV}$ (π) and $W=22.5\text{eV}$ ($\pi+\sigma$) are clearly visible in the picture.

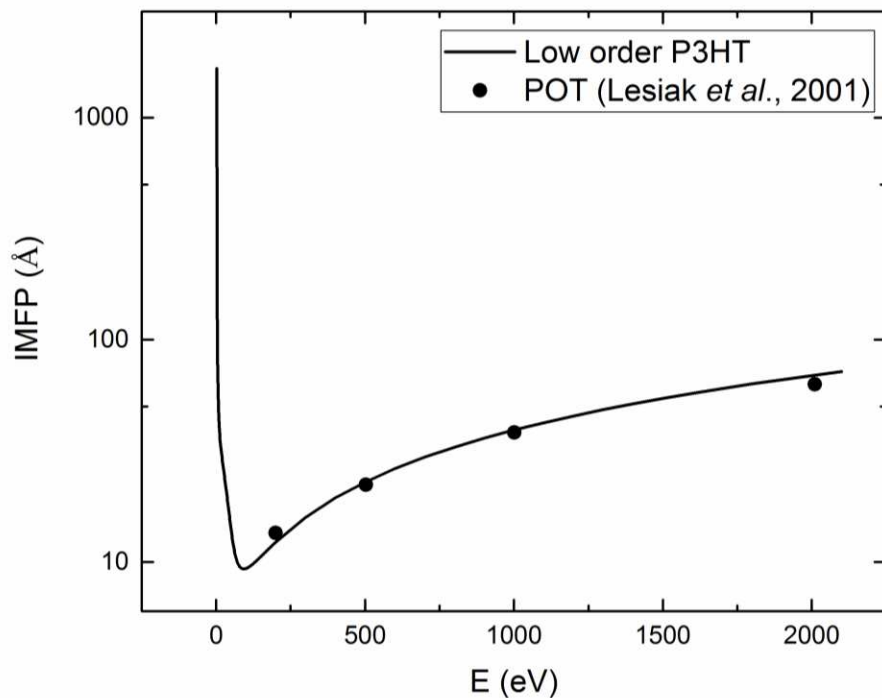


Fig.2. Inelastic mean free path of electrons in low order P3HT as a function of the incident electron kinetic energy E , calculated including only electron-electron interactions (solid line). For comparison also the measured inelastic mean free path of electrons in Poly(3-octylthiophene) (POT), a polymer structurally very similar to P3HT, is reported for a few selected values of the electron energy higher than 200eV (filled circles).⁵⁵ As the energy decreases toward the energy of the band gap ($E_{\text{gap}}=2.2\text{eV}$), the calculated IMFP quickly increases showing that the probability of inelastic scattering due to only the electron-electron interactions goes to zero.

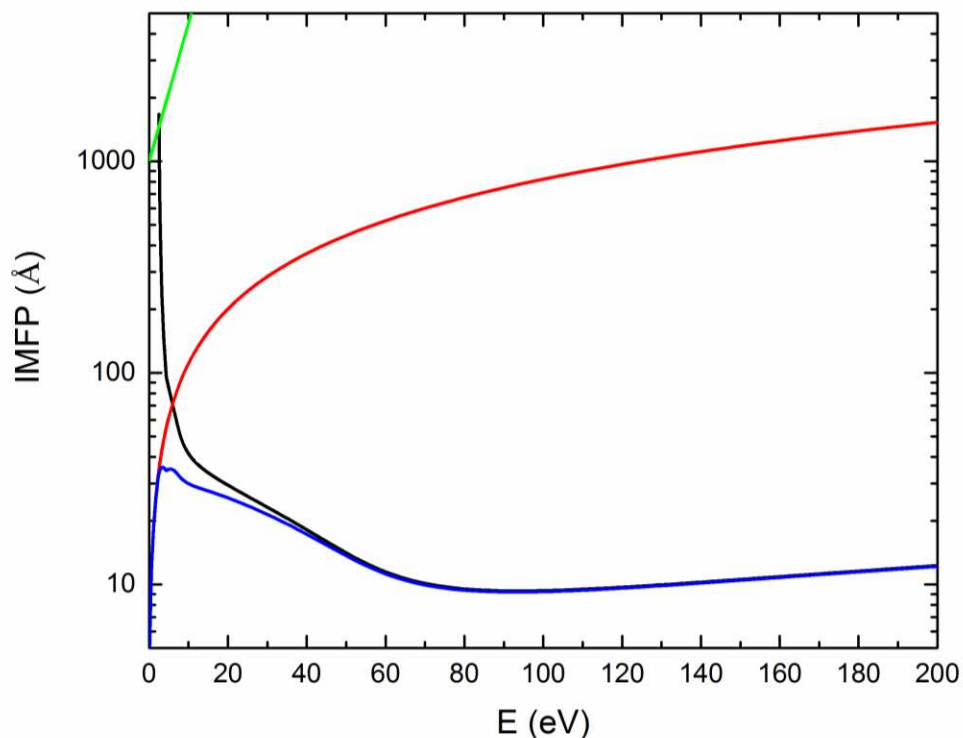


Fig.3. (Color online) Comparison between electron-electron, electron-phonon, and trapping related IMFP and the resulting total IMFP in low order P3HT. Black line: electron-electron interaction. Red line: electron-phonon interaction. Green line: trapping phenomena. Blue line: all the interactions (electron-electron, electron-phonon, trapping) included. The probability of interaction is proportional to the reciprocal of the IMFP. Below 6eV the probability of electron-phonon interaction becomes higher than the probability of electron-electron interaction. Below 2.2eV (energy of the band gap) the probability of electron-electron interaction becomes equal to zero, while the probability of electron-phonon interaction increases. Trapping only plays a minor role, thus the overall IMFP is dominated by electron-phonon interactions for electrons below 6eV. Note that the effects of the various inelastic scattering cross-sections on the energy losses are very different. While the electron-phonon excitation leads to an energy loss of 50meV, the electron-electron excitation leads to an energy loss of several eV, even below 6eV.

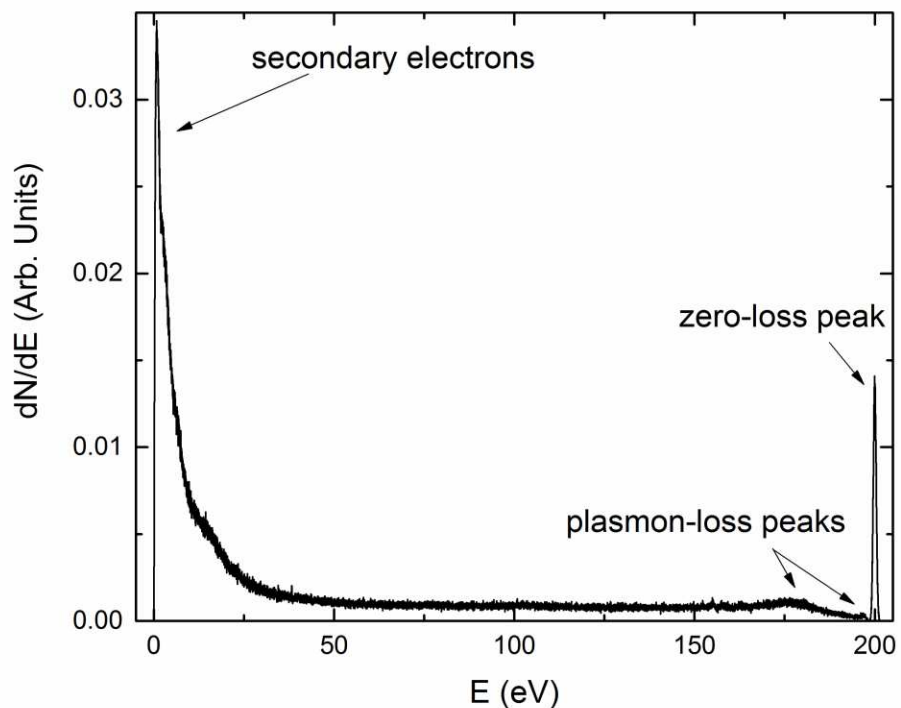


Fig.4. Monte Carlo simulation of the energy distribution of electrons emerging from the surface of low order P3HT when the primary electron energy E_0 is 200 eV. The peaks of secondary electrons, and of reflected electrons with both zero loss and plasmon losses, are clearly visible in the spectrum. A shoulder can be observed in the very low energy part of the spectrum (in the secondary electron regime), in the energy range ~ 10 -24 eV, which we attribute to emission from excited $\pi+\sigma$ plasmon levels (see the shape of the ELF in Fig. 1). The zero of the energy scale of the emerging electrons is located at the vacuum level.

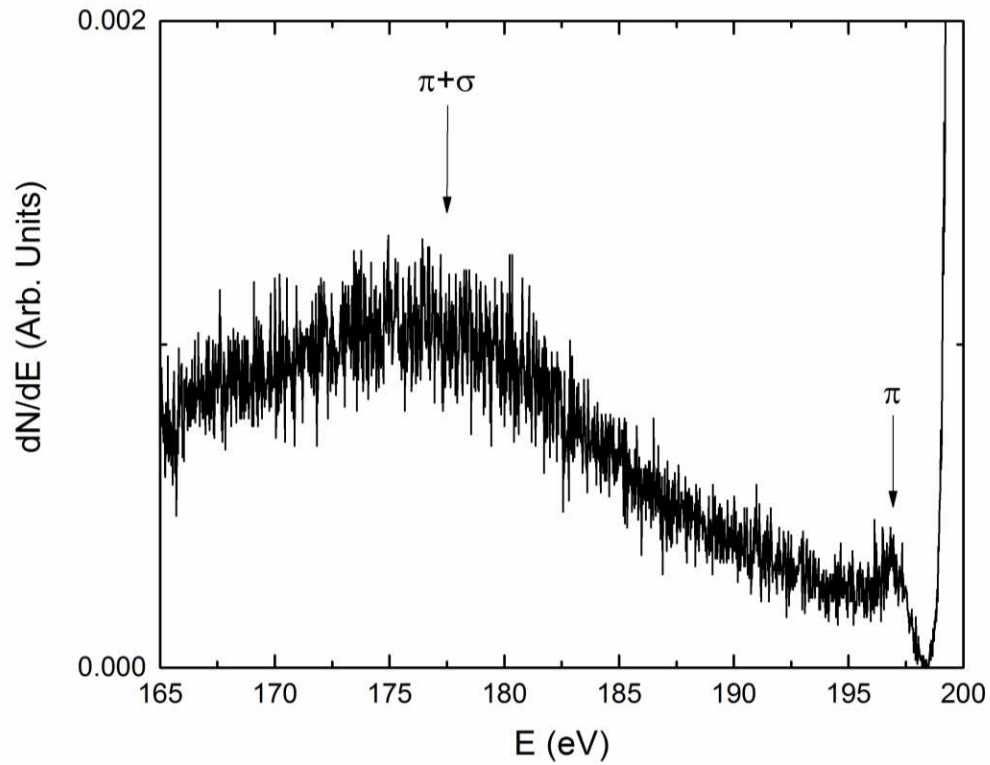


Fig.5. Monte Carlo simulation of the energy distribution of electrons emerging from the surface of low order P3HT close to the zero-loss peak (filtering depth $D=2.5\text{nm}$). Primary electron energy E_0 is 200eV. The elastic peak from zero-loss reflected electrons can be observed at 200 eV. Peaks from reflected electrons with plasmon losses of $\sim 2.8\text{eV}$ (π) and $\sim 22.5\text{eV}$ ($\pi + \sigma$) are clearly visible in the spectrum. The zero of the energy scale is located at the vacuum level.

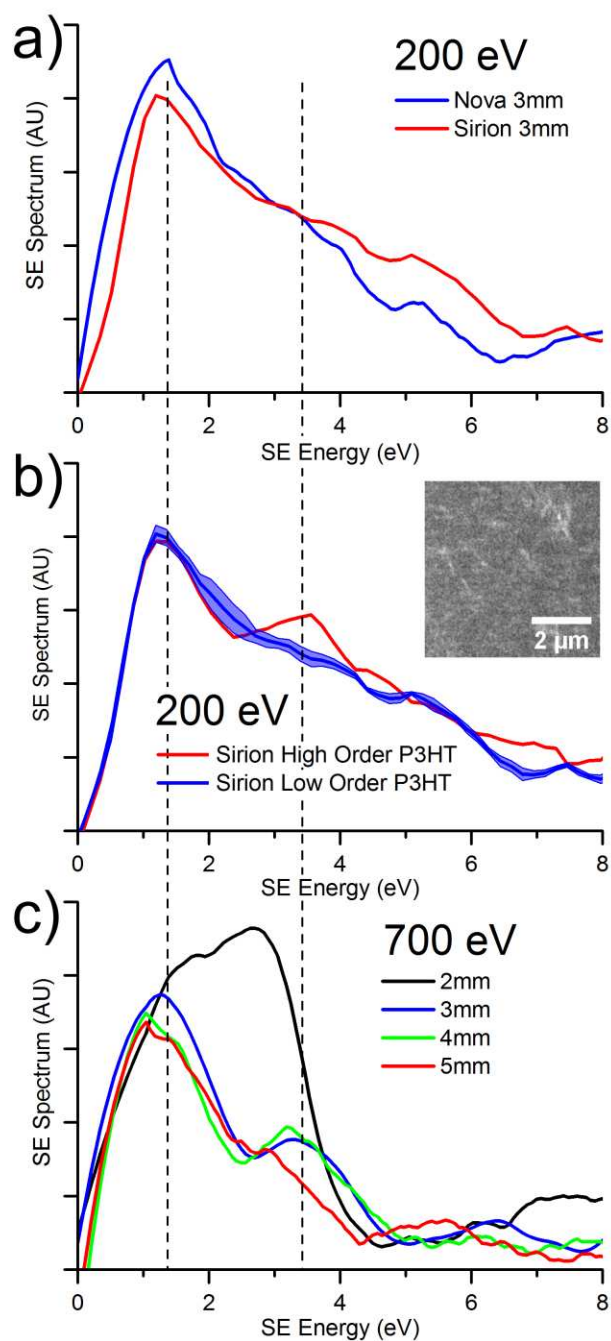


Fig. 6. (Color online) Demonstration of the effects of microscope (a), level of ordering (b) and working distance (c) on the shape of a P3HT SE spectrum. The spectra in (a) were collected with a 200 eV primary beam while those in (b) and (c) were collected with a 700 eV primary beam energy (in NOVA). The inset image in part (b) demonstrates the order-related image contrast from an annealed P3HT sample when imaged using only SE with energies ~ 5 eV and below. The vertical dashed lines indicate the coincidence of peak positions for both 200 eV and 700 eV primary electron beam when using a 3 mm working distance.

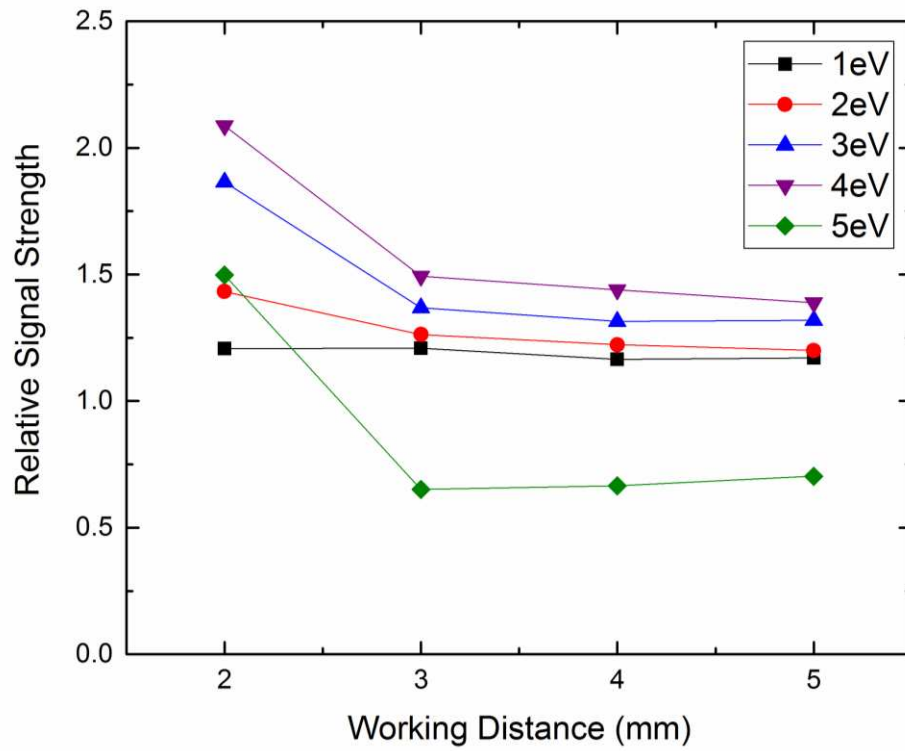


Fig 7. (Color online) The signal relative to the signal at 0 eV for various cut-off energies as a function of working distance. We take this ratio as an indicator for the detection efficiency. The higher the SE cut-off energy the stronger the reduction in detection efficiency with increased working distance.

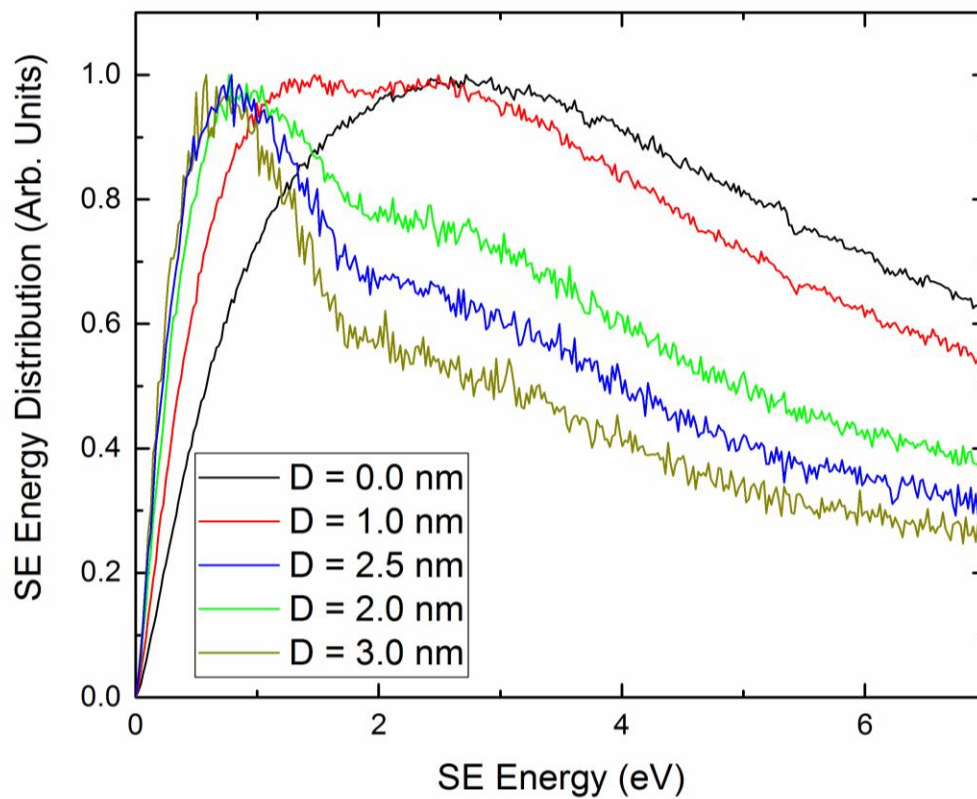


Fig.8. (Color online) Secondary electron spectra of low order P3HT for different values of the filtering depth D , for an incident electron energy $E_0=200$ eV. The zero of the energy scale of the emerging electrons is located at the vacuum level. All the distributions are normalized to have the same maximum value.

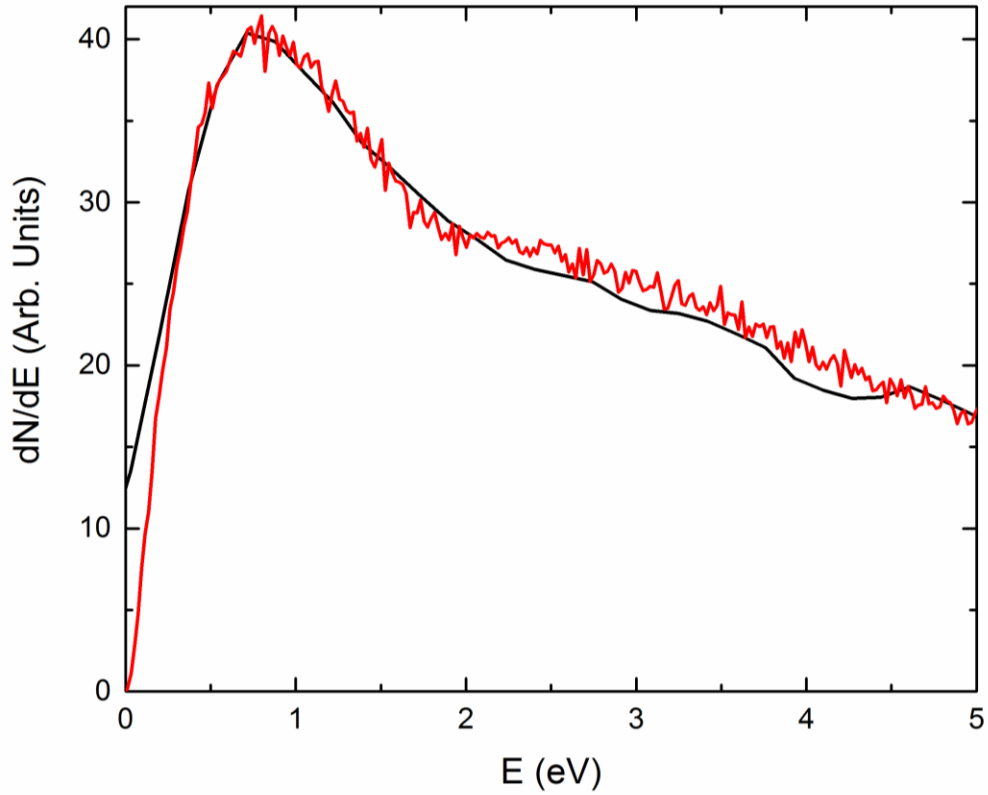


Fig.9. (Color online) Secondary electron spectrum (filtering depth $D=2.5\text{nm}$) of low order P3HT, for an incident electron energy $E_0=200\text{eV}$. The Monte Carlo results (red line) are compared with the experimental data of the un-annealed sample (black line). The zero of the energy scale of the emerging electrons is located at the vacuum level.

TABLE 1 Table Best fit parameters of the Drude-Lorentz sum for the calculation of the ELF of low order P3HT. n = oscillator index. W_n =energy of the n^{th} oscillator, relating to the plasmon excitation energy. Γ_n =width of the n^{th} oscillator. A_n =strength of the n^{th} oscillator.

n	W_n (eV)	Γ_n (eV)	A_n
1	2.80	0.913	0.0338
2	22.5	15.0	0.530

Supporting Information

Secondary electron spectra of semi-crystalline polymers – a novel polymer characterisation tool?

Maurizio Dapor¹, Robert C. Masters², Ian Ross³, David Lidzey⁴, Andrew Pearson⁵, Isabel Abril⁶, Rafael Garcia-Molina⁷, Jo Sharp², Marek Unčovský⁸, Tomas Vystavel⁸, Filip Mika⁹, Cornelia Rodenburg²

¹European Centre for Theoretical Studies in Nuclear Physics and Related Areas (ECT*-FBK) and Trento Institute for Fundamental Physics and Applications (TIFPA-INFN), via Sommarive 18, I-38123 Trento, Italy

²Department of Materials Science and Engineering, University of Sheffield, Mappin Street, Sheffield S1 3JD, UK

³Department of Electronic and Electrical Engineering, University of Sheffield, Mappin Street, Sheffield S1 3JD, UK

⁴Department of Physics and Astronomy, University of Sheffield, Hounsfield Road, Sheffield, S3 7RH, UK

⁵Department of Physics, University of Cambridge, Cavendish Laboratory, 19 JJ Thomson Avenue, Cambridge CB3 0HE, UK.

⁶Departament de Física Aplicada, Universitat d'Alacant, E-03080 Alacant, Spain

⁷Departamento de Física - Centro de Investigación en Óptica y Nanofísica, Regional Campus of International Excellence "Campus Mare Nostrum", Universidad de Murcia, E-30100 Murcia, Spain

⁸FEI Company, Vlastimila Pecha 1282/12, 627 00 Brno, Czech Republic

⁹ Laboratories for Electron Microscopy and Image Analysis, ISI AS CR, v.v.i.
Královopolská 147, 612 64 Brno

From [SI 1] it is apparent that the complex dielectric function of P3HT depends on the ordering of the material. As such optical measurements only cover a very small energy range, TEM-EELS was carried out.

A raw spectrum EELS spectrum is shown in Figure S1. The position of the zero-loss peak was determined to calibrate the zero energy loss position. The FWHM of the zero loss peak is 0.7eV.

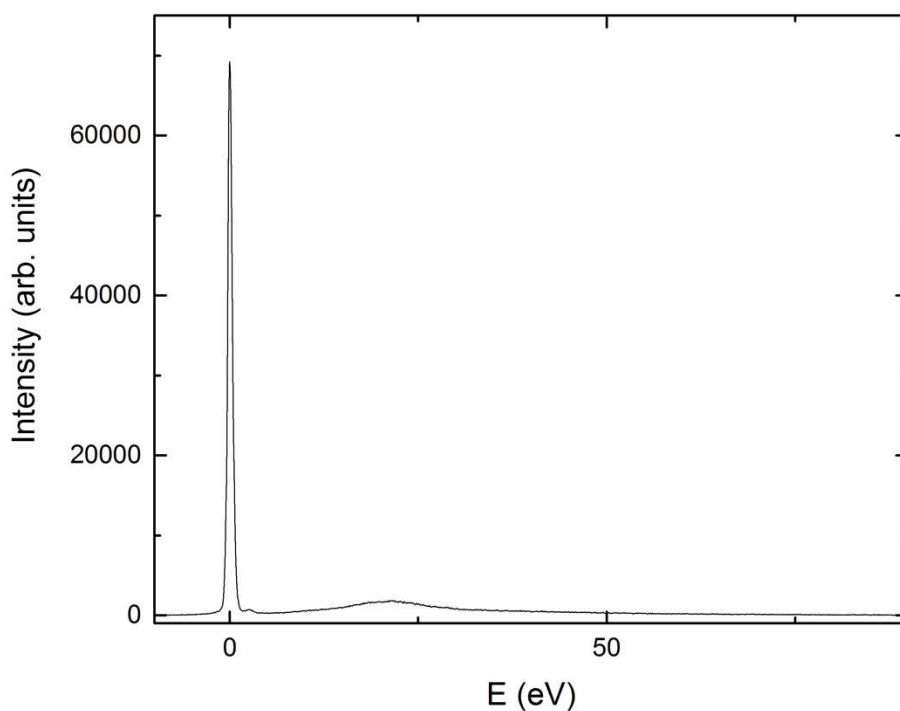


Figure E1: EELS raw data including the elastic peak (low order P3HT sample).

In order to obtain the ELF plural scattering needs to be removed first. We used the Fourier Log method, with a fitting range from 0 eV to 2.8eV. Kramers-Kronig Analysis was then carried out using measured convergence semi-angles (7.83 mrad) and collection semi-angle of 0.33 mrad, with 10 iterations. The required optical refractive index was used as fitting parameter in order to obtain the closest match possible to literature data (from optical measurements) e.g. $n=1.45$ for low order P3HT and $n=1.9$ for high order P3HT [SI 1]. With this method we also obtain as a result a film thickness, which is 115 nm and 91 nm, respectively which are both within our expectations of film thickness as measured by AFM. To further validate or ELF result we compare the related dielectric function parameters we obtain on our materials to those published by other groups in Figure S2. Although, this paper focuses on simulating LO P3HT secondary

electron spectra we include the HO EELS data in order to verify our method for the derivation of the ELF from our EELS data.

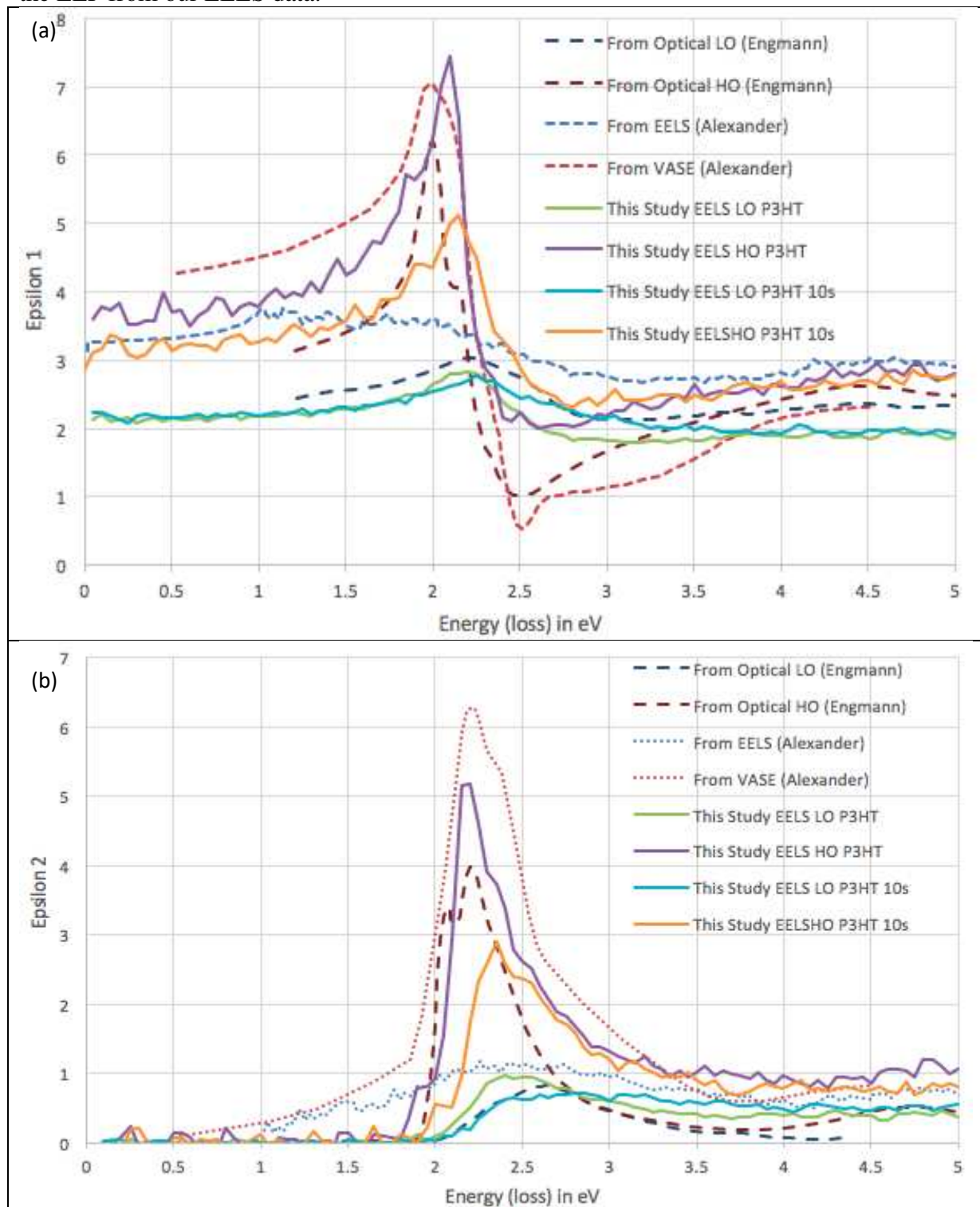


Figure S2 (a) Comparison of Epsilon 1 of P3HT derived for different materials and by different methods, (b) Comparison of Epsilon 2 of P3HT derived for different materials, electron doses and and by different methods.

In Figure S2 the match for both epsilon 1 and epsilon 2 on high order and low order P3HT in our study is fairly good in comparison to the match found between the VASE data and those derived from the EELS spectra in [SI 2]. We further note, that the data derived from EELS in [SI 2] for energies larger than 2 eV are between our low order and high order data. This is expected as most P3HT films contain both low order and high order domains as shown in [SI 3]. Thus, for this energy region our ELF data match very well that reported in [SI 2], in spite of using 300 keV electrons in our experiments. We did observe that an increased electron dose resulted in a shift of the maximum and a reduced gradient at the onset, also reported in [SI 4] even for 60keV electron exposure for both HO and LO P3HT. Therefore, only the ELF derived from data that were collected within the first second are used as input for our simulations. The effect of the prolonged exposure can be seen in Figure S3, in which the ELF derived in our study is compared to [E3].

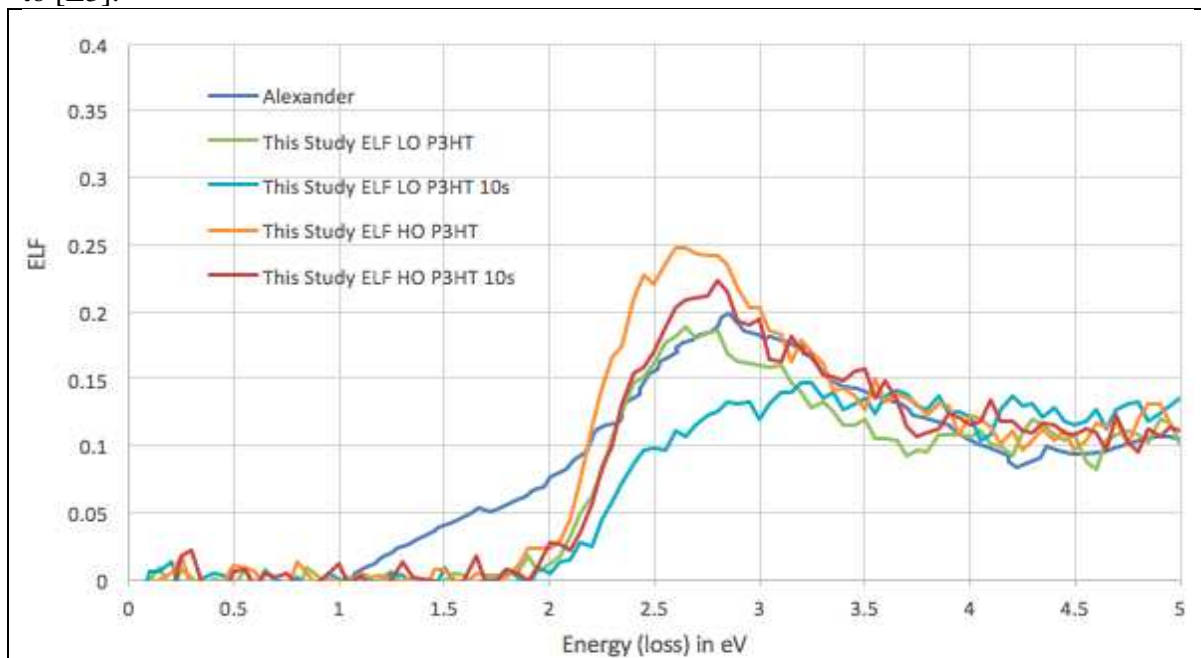


Figure S3 ELF for HO and LO P3HT, including effects of prolonged beam exposure. The data are compared to those presented in [E3].

The peak for for HO and LO P3HT is observed at 2.65eV, at the same position as reported in [SI 5] for low doses at 60 keV. The peak at 2.65 eV corresponds to the P3HT optical absorption signal and as pointed out in [SI 5] the intensity of this peak can be considered as a measure of structural degradation of the P3HT polymer chains. The time series presented in [SI 5] also show a shift in peak position towards higher energies with increased electron exposure again this is visible on our data. Given that our observed peak positions match the expected value of 2.65 eV (for a 1s electron exposure time) we are quite confident that our band gap values reflect the undamaged polymer in both LO and HO P3HT and are not unduly distorted by our ZLP removal procedure.

The optical absorption data derived from the EELS data are shown in Figure S4a and were used to determine the band gap through Tauc [SI 5] analysis, see Figure S4b.

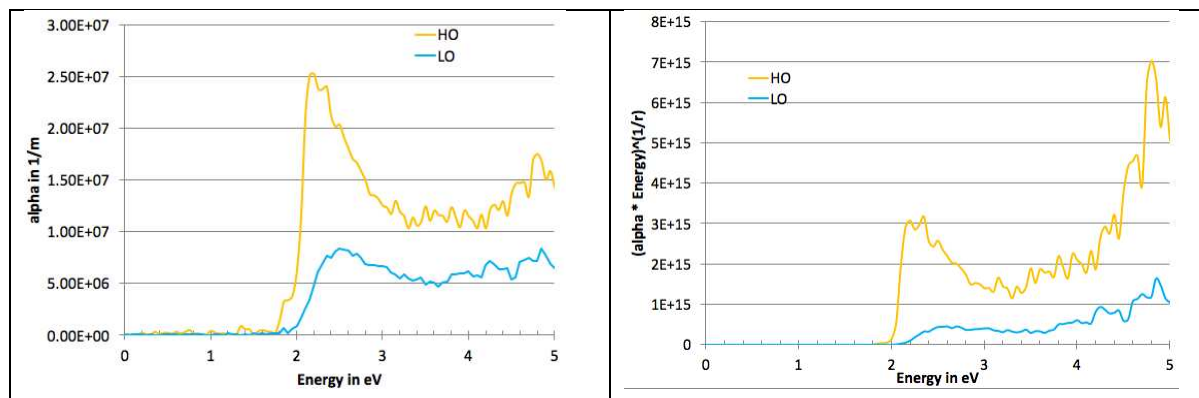


Figure S4: (a) optical absorption coefficient derived from EELS data for HO and LO P3HT and (b) Tauc plot with $r=0.5$. A clear difference in band gap between HO and LO P3HT is visible.

The Secondary Electron spectra also for LO and HO material are compared in Figure S5. There are two notable differences between these spectra: (1) the higher intensity of the main peak for the LO P3HT compared to HO P3HT, and (2) a more pronounced feature at an energy of 3.5 eV above the vacuum level. Thus confirming that changes in the complex dielectric function (notably the band gap), are reflected in the experimental secondary electron emission spectra.

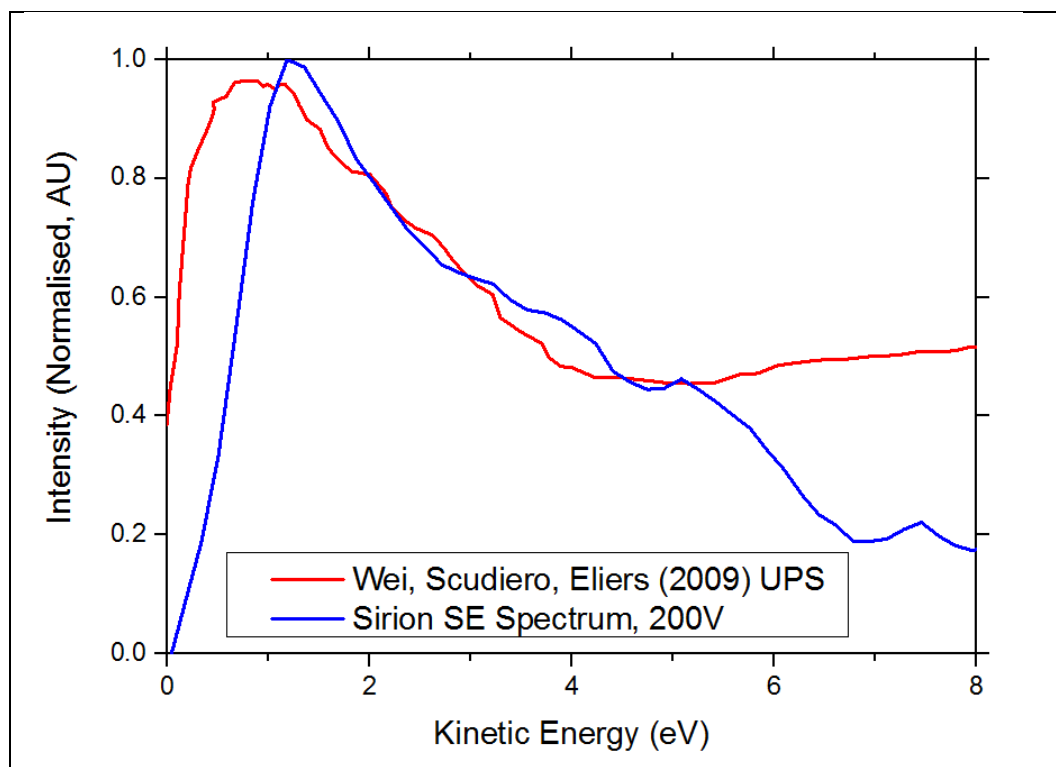


Figure S5: The experimentally measured secondary electron emission spectra compared with literature UPS spectrum [SI 6]

Ordering in the P3HT film can be probed by UV-visible absorption spectroscopy. Specifically, the ratio of intensity of the first peak (at ~ 2.05 eV) to the second peak (at ~ 2.25 eV) is a measure of the average interchain coupling or conjugation length in the film, and by implication the level of molecular ordering [SI 7]. From this, it can be observed in Figure S6 that the ‘aged’ P3HT sample demonstrates significantly greater levels of molecular ordering than the film cast from a fresh chloroform solution. This is the basis for our definition of ‘high-’ and ‘low-’ order P3HT, even though it is clear from the Figure that the as-cast film from fresh chloroform nonetheless does demonstrate a degree of crystalline aggregation.

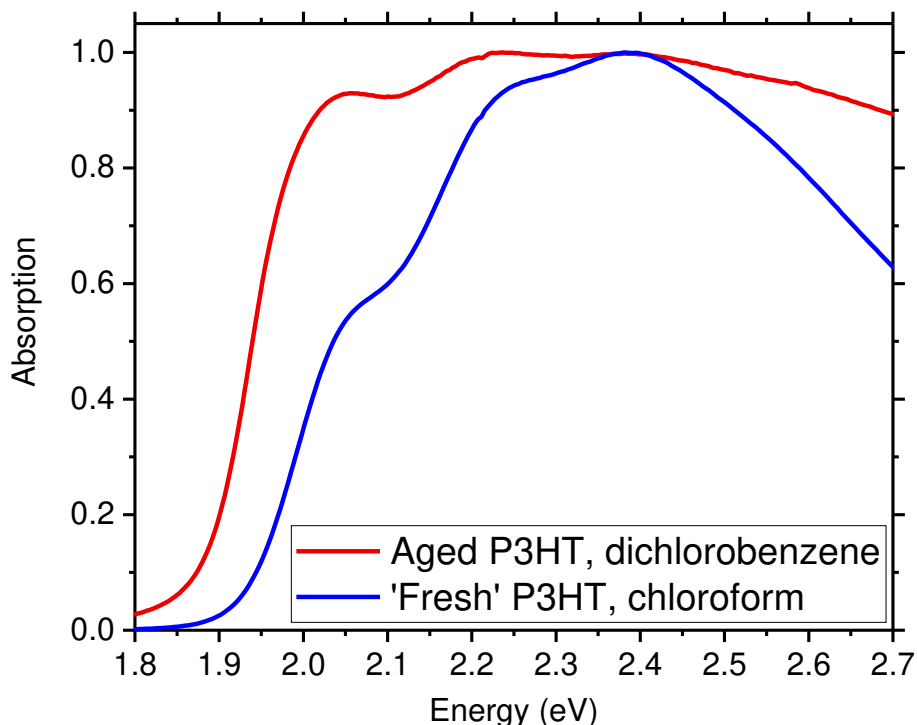


Figure S6: UV-visible absorption spectra of P3HT samples, spin-cast from ‘fresh’ chloroform solution, and blade-coated from aged dichlorobenzene solution.

P3HT films were imaged at $E_0 = 350$ eV with a FEI Magellan SEM, and features believed to reflect surface crystallinity were highlighted when imaged with energy-filtered SEs. Energy-selective detection of SEs was performed as described in [SI 8], by altering the bias, M , on the mirror electrode that forms part of the TLD assembly on the Magellan SEM. Whilst this particular SEM has not been calibrated for SE spectroscopy (meaning the value of M cannot be reliably linked to a detected SE energy), in this case a negative bias of increasing magnitude results in the detection of SEs with increasing energy. The P3HT film as imaged with gradually increasing average SE energy is shown in Fig. S7a-c, with a conventional SE image of the same area shown in Fig. S7d. Features with the appearance of crystallites or fibrils at the surface, a few hundred nm in size, can be observed more clearly in the energy-filtered SE images in comparison with the conventional, unfiltered SE image. This may represent the different SE spectrum

emitted by crystalline phases of P3HT, which could possibly be exploited by energy-filtered SE imaging for improved-contrast phase mapping (a similar concept to that demonstrated in [SI 8]).

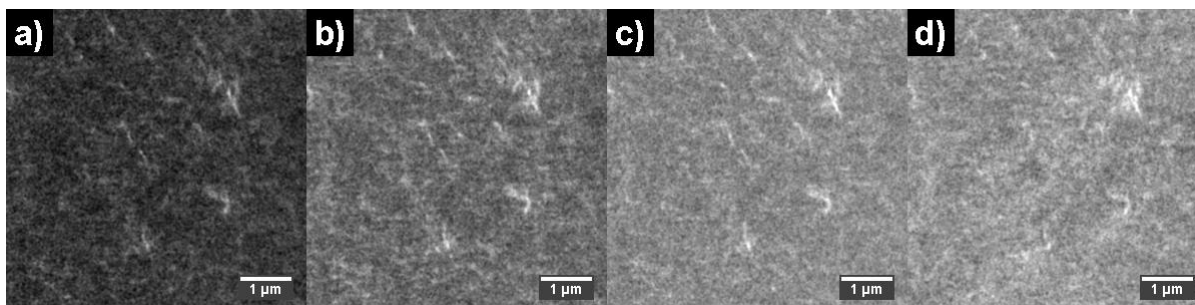


Figure S7: Images of P3HT acquired at $E_0 = 350\text{eV}$ with a FEI Magellan SEM, with images captured with increasing average SE energy from a) to d). Part a) was captured with $M = -2\text{V}$; b) with $M = -6\text{V}$; and c) with $M = -14\text{V}$. Part d) shows the film as imaged in a conventional SE imaging mode with no energy-filtering parameters in place.

The shape of the spectra is also influenced by the working distance, due to angle dependant detection efficiency, in conjunction with critical angle considerations for the internal SE. SE approaching the surface with angles larger than the critical angle can not be emitted. It is evident from Figure S8 that the critical angle shows a strong dependence on the internal SE energy in the energy region of interest in this work.

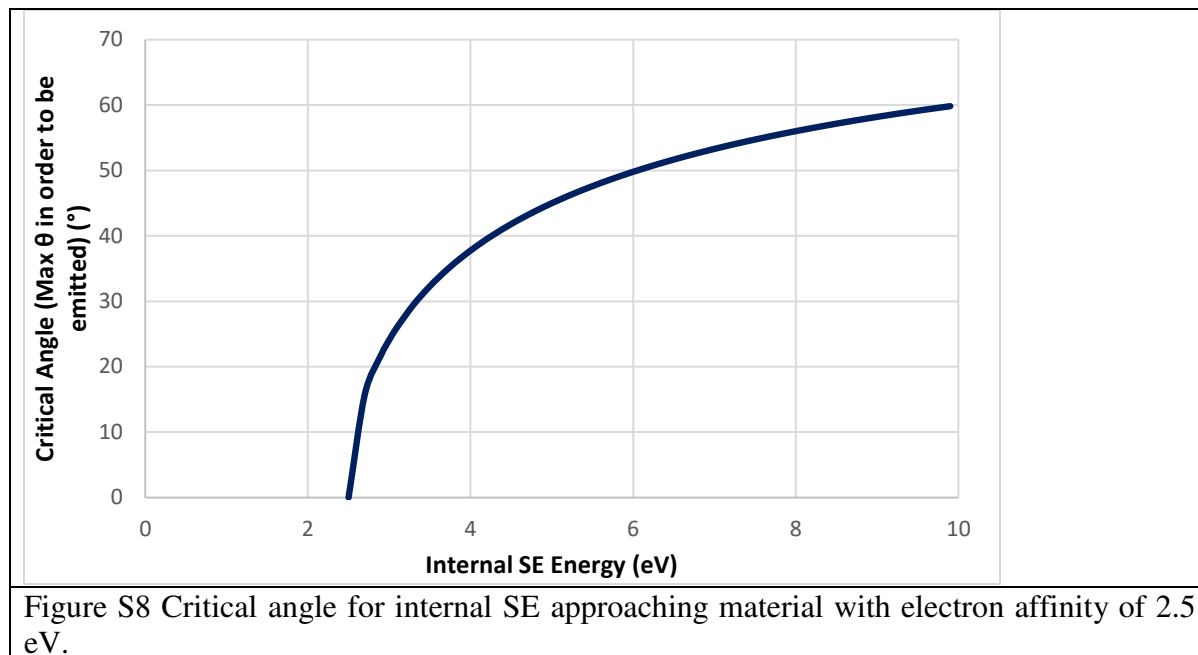


Figure S8 Critical angle for internal SE approaching material with electron affinity of 2.5 eV.

Supporting references:

- [SI 1] S. Engmann, V. Turkovic, P. Denner, H. Hoppe, and G. Gobsch, *J. Polymer Science B: Polymer Physics* 50 (2012) 1363
- [SI 2] J. A. Alexander, F. J. Scheltens, L. F. Drummy, M. F. Durstock, J. B. Gilchrist, S. Heutz, and D. W. McComb, *J. Mater. Chem. A* 4 (2016) 13636
- [SI 3] Q. Wan et al, *Ultramicroscopy* 171, (2016), 126–138
- [SI 4] M. Pfannmöller et al. *Synthetic Metals* 161(2012) 2526-2533
- [SI 5] J. Tauc, R. Grigorovici, and A. Vancu, *Phys. Status Solidi B* 15 (1966) 627
- [SI 6] H. Wei, L. Scudiero, H. Eilers, *Appl. Surf. Sci.* 255 (2009) 8593-8597
- [SI 7] J. Clark, C. Silva, R. Friend and F. Spano, *Phys. Rev. Lett.* 98 (2007) 206406
- [SI 8] R. C. Masters, A. J. Pearson, T. S. Glen, F. C. Sasam, L. Li, M. Dapor, A. M. Donald, D. G. Lidzey and C. Rodenburg, *Nat. Comms.* 6 (2015), 6928